

## Extended Hubbard model describing small multidot arrays in bilayer graphene

Angelika Knothe<sup>1</sup> and Guido Burkard<sup>2</sup>

<sup>1</sup>Institut für Theoretische Physik, Universität Regensburg, D-93040 Regensburg, Germany

<sup>2</sup>Department of Physics, University of Konstanz, D-78457 Konstanz, Germany



(Received 19 January 2024; accepted 16 May 2024; published 3 June 2024)

We set up and parametrize a Hubbard model for interacting quantum dots in bilayer graphene and study double dots as the smallest multidot system. We demonstrate the tunability of the spin and valley multiplets, Hubbard parameters, and effective exchange interaction by electrostatic gate potentials and the magnetic field. Considering both the long- and short-range Coulomb interactions, we map out the various spin and valley multiplets and calculate their energy gaps for different dot sizes and interdot separations. For half-filling and large valley splittings, we derive and parametrize an effective Heisenberg model for the quantum dot spins.

DOI: 10.1103/PhysRevB.109.245401

### I. INTRODUCTION

Gate-defined nanostructures in gapped bilayer graphene (BLG) have emerged as promising platforms for quantum confinement and quantum technologies. Recent advancements in experimental techniques have enabled the successful manipulation and characterization of quantum dots (QDs) in BLG [1–19]. These achievements range from identifying the single-particle [1,2,4,19] and two-particle states [10,12] in a BLG QD to the measurement of spin [7,13,14] and valley [20] lifetimes. To scale up BLG QD systems for quantum information setups and to fully understand the material-dependent features observed in the QDs, it is necessary to develop a theoretical framework encompassing multidot systems.

In this work, we address this need by setting up a generalized Fermi-Hubbard Hamiltonian for multiple interacting BLG QDs. Building upon successful microscopic models developed for individual QDs [4,5,10,12,21–25], we parametrize the Hamiltonian to capture the essential system characteristics. We then study the low-energy states and Hubbard parameters of double-QDs, as illustrated in Fig. 1.

The theoretical description of multidot systems is paramount for comprehending the recent and ongoing experiments in the field [20,26–31]. Furthermore, the investigation of coupled QDs holds promise for spin and valley qubit formation and control [32,33], which are essential elements in quantum computing [34–40]. Beyond these immediate applications, our research also explores an extended Hubbard model incorporating long-range interactions and diverse spin and valley states that can be tuned by adjusting interdot separation and magnetic fields.

The development of such an extended model paves the way for describing larger BLG QD lattices and the use of BLG QDs for quantum simulations of exotic Fermi-Hubbard Hamiltonians. Extended Hubbard models have been shown to potentially host diverse correlation effects such as magnetism [41–53], superconducting pairing [54–58], Kondo physics [59], localization effects [60,61], translational and rotational symmetry breaking phases [48,62–66], and various topological states [67–70].

Successful realizations of multidot systems using semiconductor QDs demonstrate their potential, e.g., for quantum simulation [71–73], quantum state transfer and routing [74–78], and inducing extended interactions [79] in 1D [80–85] and 2D [86–94] QD arrays. Here, we open up alternative avenues for quantum simulation, quantum computation, and exploring emergent phenomena using confined systems in materials with complex electronic structures and enriched degrees of freedom, such as gapped BLG.

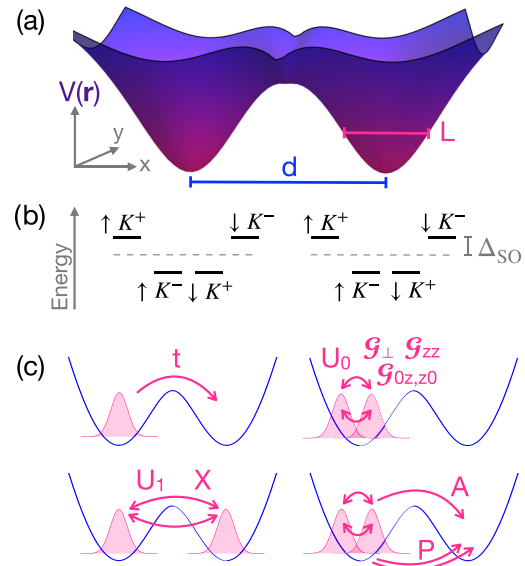


FIG. 1. (a) Two-dimensional confinement potential  $V(\mathbf{r})$  for a double-QD with dot diameter  $L$  and interdot separation  $d$ . (b) The  $B = 0$  single-particle levels comprise four spin ( $\uparrow, \downarrow$ ) and valley ( $K^\pm$ ) states per dot, separated by the spin-orbit coupling gap  $\Delta_{SO}$ . A finite perpendicular magnetic field will split these levels further proportional to their spin- and valley g-factors. (c) Single- and two-particle processes: tunneling ( $t$ ), on-site interactions ( $\propto U_0, G_{\perp}, G_{0z, z0}$ ), nearest neighbor direct ( $U_1$ ) and exchange ( $X$ ) interactions, density-assisted hopping ( $A$ ), and pair hopping ( $P$ ).

Analyzing the Hubbard model for BLG QD lattices and a double-dot as the minimal realization, we establish the following:

- (i) the low-energy states, comprising different spin and valley multiplets, whose multiplicities and splittings depend on the dot parameters,
- (ii) a microscopic understanding how different phases are driven by the competition of long-range extended Hubbard parameters and short-range interactions,
- (iii) an effective spin-spin Heisenberg model describing the low-energy double dot states in a magnetic field, with a tunable effective exchange constant.

These findings will help understanding the on-going experiments based on few-electron tunnel spectroscopy, identifying two-level regimes suitable for forming qubits, and scaling BLG QDs to larger lattices for quantum information and quantum simulation.

We obtain the results above by setting up a generalized Hubbard model for multiple BLG QDs [54,95–98],

$$\hat{H} = \sum_{j,k=1}^N t_{jk} c_j^\dagger c_k + \frac{1}{2} \sum_{h,j,k,m} U_{hjkm} c_h^\dagger c_j^\dagger c_k c_m, \quad (1)$$

where  $N$  denotes the total number of single-particle states. We parametrize this Hubbard model by evaluating the Hubbard parameters (cf. Fig. 1),

$$\begin{aligned} t_{jk} &= \langle j | \hat{H}_0 | k \rangle, \\ U_{hjkm} &= \langle h | \hat{H}_C | km \rangle, \end{aligned} \quad (2)$$

in terms of the generalized, orthonormalized single-particle states  $|j\rangle$  of the  $j$ th lattice site. These single-particle states we obtain from a microscopic model for an interacting BLG double-QD. In our microscopic model,  $\hat{H}_{\text{cont}} = \hat{H}_0 + \hat{H}_C$ , the single-particle term  $\hat{H}_0$  includes a smoothly varying potential landscape confining electrons at multiple sites (Fig. 1 for a double-QD with eight single-particle spin and valley states, hence  $N = 8$ ). The term  $\hat{H}_C$  captures material-specific electron-electron Coulomb interactions, including long-range isotropic contributions and short-range interactions sensitive to the BLG lattice and valley structure (We define all terms of the Hamiltonian and the single-particle states in detail below). Using exact diagonalization of the Hubbard Hamiltonian (1), we study the two-particle spectra and states of small multidot systems.

## II. MICROSCOPIC MODEL OF THE DOUBLE DOT AND PARAMETRIZATION OF THE HUBBARD HAMILTONIAN

Smooth confinement of charge carriers in gapped BLG has been achieved experimentally using a combination of multiple gates (typically, two split gates to confine a channel and finger gates crossing the channel on top to confine a dot) [20, 26–31,99–101]. The gates locally tune both the gap, and the charge carrier density and hence confine the charge carriers electrostatically. For a BLG double-QD as the smallest possible multidot system, we choose a smooth confinement potential  $V(\mathbf{r})$  and a spatially modulated gap  $\Delta(\mathbf{r})$  of the form depicted in Fig. 1(a),

$$V(\mathbf{r}) = V_0 V_{\text{conf}}(\mathbf{r}), \quad \Delta(\mathbf{r}) = \Delta_0 - \Delta_{\text{mod}} V_{\text{conf}}(\mathbf{r}),$$

where

$$\begin{aligned} V_{\text{conf}}(\mathbf{r}) &= \frac{1}{\cosh \sqrt{(x - x_i)^2 + y^2}/L} - V_{\text{neck}}(\tilde{x}_i), \\ V_{\text{neck}} &= \frac{1}{L^2} \frac{Z}{2x_i^2} (x - x_i)^4 \Theta(|x_i| - |x|), \end{aligned} \quad (3)$$

with  $i = l$  for  $x < 0$  (left) and  $i = r$  for  $x > 0$  (right) and  $\Theta$  is the Heaviside step function. The parameters  $V_0$  and  $\Delta_0$  in Eq. (3) describe the depth of the confinement and the BLG band gap in the absence of any spatial modulation (away from the dots), while the term proportionally to  $\Delta_{\text{mod}}$  captures the modulation of the gap towards the center of the dot (for the magnitude of the modulation  $\Delta_{\text{mod}} \approx 0.3\Delta_0$  has proven realistic in recent theoretical and experimental works [4,5,10,21]). Moreover,  $L$ , defines the diameter of the individual QDs, while  $d = x_r - x_l$  is the distance between the dots (see Fig. 1). Further,  $Z$  is a fit parameter which we choose such that the neck of the potential [102–107] is smooth at  $x = 0$ . In BLG, skew hopping between the two graphene layers breaks rotational symmetry, distinguishing between the two crystallographic directions. Below, we consider dots oriented along the  $x$  direction (corresponding to aligning them along the zigzag direction of the BLG lattice). Orientation of the dots along the  $y$  direction (aligning along the armchair direction) leads to qualitatively similar results that we provide in Appendix C. The potential and gap of Eq. (3) enter into the single-particle four-band BLG Hamiltonian [108,109],

$$H_0(\mathfrak{s}, t) = \begin{pmatrix} V - \frac{1}{2} t\Delta + \mathfrak{s}t\Delta_{\text{SO}} + \mathfrak{s}g_S\mu_B B & tv_3\pi & 0 & tv\pi^\dagger \\ tv_3\pi^\dagger & V + \frac{1}{2} t\Delta + \mathfrak{s}t\Delta_{\text{SO}} + \mathfrak{s}g_S\mu_B B & tv\pi & 0 \\ 0 & tv\pi^\dagger & V + \frac{1}{2} t\Delta + \mathfrak{s}t\Delta_{\text{SO}} + \mathfrak{s}g_S\mu_B B & \gamma_1 \\ tv\pi & 0 & \gamma_1 & V - \frac{1}{2} t\Delta + \mathfrak{s}t\Delta_{\text{SO}} + \mathfrak{s}g_S\mu_B B \end{pmatrix}, \quad (4)$$

where  $\pi = p_x + ip_y$ ,  $\pi^\dagger = p_x - ip_y$ ,  $\mathbf{p} = -i\hbar\nabla - \frac{e}{c}\mathbf{A}$ , with elementary charge,  $e > 0$ , speed of light  $c$  and vector potential  $\mathbf{A} = \frac{B}{2}(-y, x, 0)$  in a symmetric gauge for an out-of plane magnetic field  $B$ . The Zeeman coupling of the two spin states,  $\uparrow, \downarrow$  ( $\mathfrak{s} = \pm 1$ ), is proportional to the spin  $g$  factor  $g_s$  and the Bohr magneton  $\mu_B$ . Further,  $\Delta_{\text{SO}}$  is a Kane-Mele type spin-orbit-coupling gap enhanced by zero-point vibrations [6,15,110,111],  $v = 1.02 \times 10^6$  m/s,  $v_3 \approx 0.12v$ , and  $\gamma_1 = 0.38$  eV. The above Hamiltonian is written in the basis  $\Phi_{K^+} = (\phi_A, \phi_{B'}, \phi_{A'}, \phi_B)$  or  $\Phi_{K^-} = (\phi_{B'}, \phi_A, \phi_B, \phi_{A'})$  of states on the four BLG sublattices in the two valleys,  $K^\pm$  (indexed by  $t = \pm 1$ ). Confinement models of similar shape have been used previously successfully to describe individual, single QDs in BLG [4,10,12,21–23].

For the electron-electron interactions in Eqs. (1) and (2),  $\hat{H}_C = \hat{\Lambda} + \hat{\Upsilon}$ , we take into account the screened long-range Coulomb interaction,  $\hat{\Lambda}$ , and short-range interactions,  $\hat{\Upsilon}$ , where the latter break sublattice and valley symmetry on the lattice scale. The

short-range interactions stem from symmetry breaking fluctuations and favour states with spontaneously broken symmetries [112–115]. The respective corresponding matrix elements, Eq. (2), read

$$\langle h:i_1s_1t_1, j:i_2s_2t_2 | \hat{\Lambda} | m:i_4s_4t_4, k:i_3s_3t_3 \rangle = \delta_{s_1s_4}\delta_{s_2s_3}\delta_{t_1t_4}\delta_{t_2t_3} \int d\mathbf{r} d\mathbf{r}' [\Psi_{h:i_1}^*(\mathbf{r})\Psi_{j:i_2}^*(\mathbf{r}')] U_{\text{scr}}(\mathbf{r} - \mathbf{r}') [\Psi_{k:i_3}(\mathbf{r}')\Psi_{m:i_4}(\mathbf{r})],$$

$$U_{\text{scr}}(\mathbf{q}) = \frac{e^2}{4\pi\epsilon\epsilon_0} \frac{2\pi}{q(1+qR_\star)}, \quad U_{\text{scr}}(\mathbf{r}) = \int \frac{d^2q}{(2\pi)^2} e^{i\mathbf{q}\cdot\mathbf{r}} U_{\text{scr}}(\mathbf{q}), \quad (5)$$

$$\langle h:i_1s_1t_1, j:i_2s_2t_2 | \hat{\Upsilon} | m:i_3s_4t_4, k:i_4s_3t_3 \rangle = \delta_{s_1s_4}\delta_{s_2s_3}\delta_{hjm}\tilde{\Upsilon}_{hjm} \begin{cases} \mathcal{G}_{zz} + \mathcal{G}_{z0} + \mathcal{G}_{0z}, & \text{if } t_1 = t_2 = t_4 = t_3, \\ \mathcal{G}_{zz} - \mathcal{G}_{z0} - \mathcal{G}_{0z}, & \text{if } t_1 = t_4 = t, t_3 = t_2 = t', t \neq t' \\ 4\mathcal{G}_\perp, & \text{if } t_1 = t_3 = t, t_2 = t_4 = t', t \neq t', \end{cases}$$

$$\tilde{\Upsilon}_{hjm} = \int d\mathbf{r} \Psi_{h:i_1}^*(\mathbf{r})\Psi_{j:i_2}^*(\mathbf{r})\Psi_{k:i_3}(\mathbf{r})\Psi_{m:i_4}(\mathbf{r}). \quad (6)$$

Here,  $|j:ist\rangle$  denotes the state with orbital quantum number  $i$ , spin  $s$ , and valley index  $t$  of the  $j$ th QD.

In the screened long-range interaction between the particles in the QDs [21,112,116], Eq. (5),  $\epsilon_0$  denotes the vacuum permittivity,  $\epsilon$  is the encapsulating substrate material's dielectric constant, and the screening length  $R_\star = \sqrt{32\hbar\kappa}/\sqrt{m\Delta_0}$  accounts for gapped BLG's polarizability  $\kappa^2 = 2me^4/(4\pi\epsilon_0\epsilon\hbar\sqrt{\Delta_0})^2$  with  $m = \gamma_1/2v^2$  the effective mass [109,112] and  $\Delta_0$  the BLG gap.

The short-range interactions, Eq. (6), are parametrized by the coupling constants,  $\mathcal{G}_{\mu\nu}$ . Specifically, intervalley scattering generates the coupling  $\mathcal{G}_{xx} = \mathcal{G}_{yy} = \mathcal{G}_{xy} = \mathcal{G}_{yx} =: \mathcal{G}_\perp$ , intravalley scattering leads to  $\mathcal{G}_{zz}$ , and “current-current” interactions induce  $\mathcal{G}_{0z}$  and  $\mathcal{G}_{z0}$  [117] (the latter favoring states with spontaneously broken time-reversal invariance [115]). These short-range coupling constants mentioned above have been shown both theoretically [21,23] and experimentally [12] to be crucial for providing an accurate description of the interacting few-particle confined states in BLG QDs.<sup>1</sup>

*Single, isolated QDs*, have been calculated and discussed previously in Refs. [4,5,10,12,21–23]. A single dot's orbital spectrum and wave functions,  $\varphi_i(\mathbf{r})$ , are readily obtained from Eq. (4) with  $x_l = x_r = 0$  and  $V_{\text{neck}} \equiv 0$  using the numerical diagonalization methods of Refs. [21,22,118]. Each orbital level further splits into four spin and valley states (cf. Fig. 1),

$$E_{i,s,t} = E_i + st\Delta_{SO} + s\frac{1}{2}g_S\mu_BB + tg_v^i\mu_BB, \quad (7)$$

where  $E_i$  is the single-particle energy of the  $i$ th level and  $g_v^i$  is the valley  $g$  factor. The latter is a consequence of gapped BLG's nontrivial Bloch band Berry curvature entailing an topological orbital magnetic moment with opposite sign in the two different valleys [119–122]. It hence splits the valley states in a finite perpendicular magnetic field depending on the distribution of the  $i$ th level's wave function distribution in momentum space [5,21,100].

In the following, we will consider the experimentally relevant regime of weakly gapped dots for which the lowest

<sup>1</sup>Other combinations of indices  $\mu, \nu$  which do not appear equation Eq. (6) do not affect the states in gapped BLG since the corresponding fluctuations, while allowed by the symmetry of the lattice, are suppressed by the layer polarization [except the case  $\mu = \nu = 0$  which already included in Eq. (5)].

orbital level is singly-degenerate and well separated from the higher-energy states [21].<sup>2</sup> We will henceforth focus on this lowest-energy single-particle orbital and drop the orbital index and denote the lowest-orbital single-particle wave function by  $\varphi(\mathbf{r})$ . Using these orbital wave functions to write the wave functions of the left ( $l$ ) and the right ( $r$ ) single dots as  $\varphi_{l/r}(\mathbf{r}) = \varphi(x - x_{l/r}, y) e^{-i\frac{e\hbar}{\epsilon\hbar} \frac{x_{l/r}}{2}}$ , we obtain the orthonormalized orbital states of the double dot as  $(\Psi_l, \Psi_r)^T = \mathcal{O}^{-\frac{1}{2}}(\varphi_l, \varphi_r)^T$ , where the matrix elements of the overlap matrix,  $\mathcal{O}$ , are given by  $\mathcal{O}_{\alpha\beta} = \int d\mathbf{r} \varphi_\alpha^*(\mathbf{r})\varphi_\beta(\mathbf{r})$  with  $\alpha, \beta \in \{l, r\}$ .

From these orthonormalized states, we evaluate the Hubbard parameters for [36,89,96,98,123–127]

$$\begin{aligned} &\text{the single-particle tunneling, } t = \langle l:s:t | H_0 | r:s:t \rangle, \\ &\text{direct nearest-neighbor interaction,} \\ &U_1 = \langle l:s:t, r:s:t' | \Lambda | l:s:t, r:s:t' \rangle, \\ &\text{intersite exchange, } X = \langle l:s:t, r:s:t' | \Lambda | r:s:t, l:s:t' \rangle, \\ &\text{density-assisted hopping, } A = \langle l:s:t, l:s:t' | \Lambda | l:s:t, r:s:t' \rangle, \\ &\text{pair hopping, } P = \langle l:s:t, l:s:t' | \Lambda | r:s:t, r:s:t' \rangle, \end{aligned} \quad (8)$$

and the on-site interactions which are modified by  $\Upsilon$ :

$$\begin{aligned} \langle l:s:t, l:s:t' | \hat{H}_C | l:s:t, l:s:t' \rangle &= U_0 + \mathfrak{J}[\mathcal{G}_{zz} + tt'(\mathcal{G}_{z0} + \mathcal{G}_{0z})], \\ \langle l:s:t, l:s:t' | \hat{H}_C | l:s:t', l:s:t \rangle &= 4\mathfrak{J}\mathcal{G}_\perp, \end{aligned} \quad (9)$$

with  $U_0 = \langle l:s:t, l:s:t' | \Lambda | l:s:t, l:s:t' \rangle$  being the on-site Coulomb repulsion. In above Eq. (9), we dropped the indices of  $\mathfrak{J}$  in Eq. (6) as we are considering only the lowest orbital states in the left or right dot, respectively. We relate the Hubbard parameters in Eqs. (8) and (9) to the generalized Hubbard Hamiltonian of Eq. (1) in Appendix A.

Equipped with the Hubbard Hamiltonian, Eq. (1), thus parameterized for the BLG double dot, we study its two-electron low-energy states by exact diagonalization using the python package qmeeq [128]. In choosing realistic values for the material parameters, we base our discussion on recent experiments [12,23] in BLG QDs measuring the various interaction-induced and field-induced splitting scales. For the numerical

<sup>2</sup>The generalization to considering multiple orbitals per dot is straightforward and will be explored in future work.

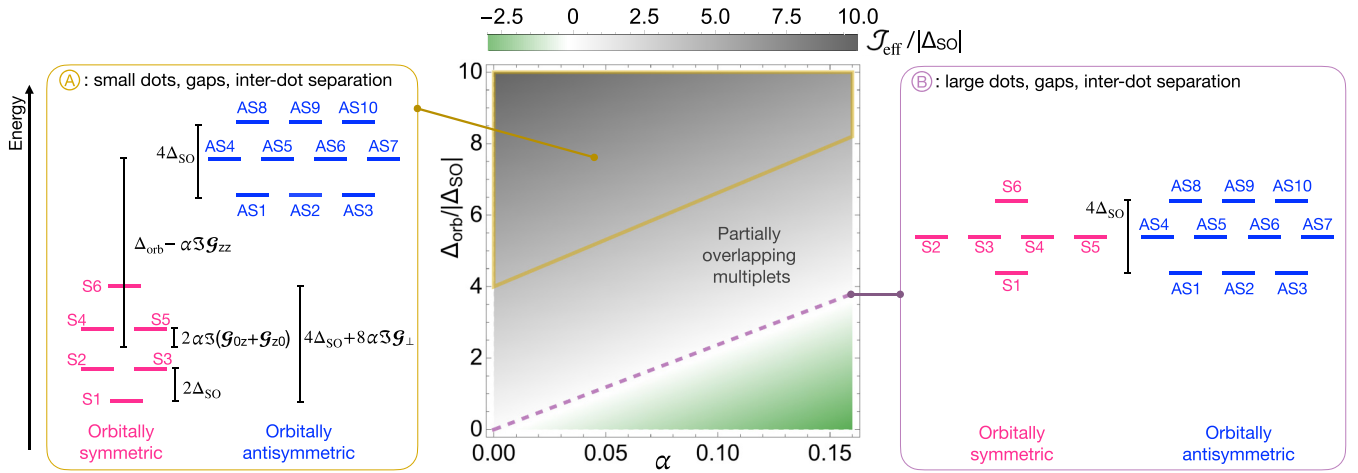


FIG. 2. The ordering and multiplicity of the low-energy states of two interacting electrons in a BLG double dot [Eqs. (10) and (16)] varies depending on the system parameters. The spin and valley multiplets can be fully separated, partially overlapping, or fully overlapping, depending on the orbital splitting  $\Delta_{\text{orb}}$ , the spin-orbit gap  $\Delta_{\text{SO}}$ , and the short-range splittings [the latter being proportional to the weight of doubly occupied orbitals  $\alpha$ , cf. Eq. (12)]. In the limiting regimes of small dots, small gaps, and small interdot separation (Ⓐ, left), the orbitally symmetric and antisymmetric multiplets are well separated [meaning that there is a finite gap between states  $|S_6\rangle$  and  $|AS123\rangle$ ], while for large dots, large gaps, and large interdot distance (Ⓑ, right), the multiplets fully collapse [here we quantify the separation by an effective exchange constant  $J_{\text{eff}}$  measuring the distance between  $|S_4\rangle$  and  $|AS7\rangle$ , cf. Eq. (20)]. Orbitally symmetric and antisymmetric states are separated by  $\Delta_{\text{orb}}$ . Within the multiplets, different spin and valley states are split by  $\Delta_{\text{SO}}$  and by the short-range interactions  $\propto \alpha \Im \mathcal{G}_{\perp,0z,0}$ . For these particular level orderings, we assume  $\Delta_{\text{SO}} < 0$ ,  $\mathcal{G}_{\perp,0z,0} > 0$ ,  $\mathcal{G}_{zz} \approx 10\mathcal{G}_{\perp}$  (see text for realistic values).

results we use  $\Delta_{\text{SO}} = -0.04$  meV, [6,15,110,111]  $\Im \mathcal{G}_{\perp} \approx 0.075$  meV,  $\mathcal{G}_{0z} \approx \mathcal{G}_{z0} \approx \frac{2}{3}\mathcal{G}_{\perp}$ ,  $\mathcal{G}_{zz} \approx 10\mathcal{G}_{\perp}$ , [12,21,23] and  $\epsilon = 5$  corresponding to the order of magnitude of bulk hBN widely used as encapsulating material [124,129,130]. We provide all explicit numerical results, including other values of  $\epsilon$ , in Appendix C.

Figure 2 illustrates the different level orderings of double dot two-particle spin and valley states we find as a function of dot and gap size and interdot separation. In general, the lowest-energy two-particle states comprise a multiplet of six spin and valley states with a symmetric orbital wave function (so-called “supersinglet” states [131]), and ten states with an antisymmetric orbital wave function (“supertriplets” [131]) [12,21,23,32,132,133].

The states with symmetric orbital wave function,  $|\Psi_S\rangle$ , are given by

$$\begin{aligned} |S1\rangle &= \frac{|\Psi_S\rangle}{\sqrt{2C}} [(|+\uparrow\rangle|-\downarrow\rangle - |-\downarrow\rangle|+\uparrow\rangle) \\ &\quad + b(|+\downarrow\rangle|-\uparrow\rangle - |-\uparrow\rangle|+\downarrow\rangle)], \\ |S2\rangle &= \frac{|\Psi_S\rangle}{\sqrt{2}} [(-\downarrow\rangle|+\downarrow\rangle - |+\downarrow\rangle|-\downarrow\rangle)], \\ |S3\rangle &= \frac{|\Psi_S\rangle}{\sqrt{2}} [|+\uparrow\rangle|-\uparrow\rangle - |-\uparrow\rangle|+\uparrow\rangle], \\ |S4\rangle &= \frac{|\Psi_S\rangle}{\sqrt{2}} [|+\downarrow\rangle|+\uparrow\rangle - |+\uparrow\rangle|+\downarrow\rangle], \\ |S5\rangle &= \frac{|\Psi_S\rangle}{\sqrt{2}} [(-\uparrow\rangle|-\downarrow\rangle - |-\downarrow\rangle|-\uparrow\rangle], \\ |S6\rangle &= \frac{|\Psi_S\rangle}{\sqrt{2C}} [(|+\downarrow\rangle|-\uparrow\rangle - |-\uparrow\rangle|+\downarrow\rangle) \\ &\quad - b(|+\uparrow\rangle|-\downarrow\rangle - |-\downarrow\rangle|+\uparrow\rangle)], \end{aligned} \quad (10)$$

with  $|st\rangle$  denoting the spin ( $s = \uparrow, \downarrow$ ) and valley ( $t = +, -$ ) state and [36]<sup>3</sup>

$$|\Psi_S\rangle \approx \left[ \frac{a_1}{\sqrt{2}} (|l\rangle|r\rangle + |r\rangle|l\rangle) + a_2 (|l\rangle|l\rangle + |r\rangle|r\rangle) \right]. \quad (11)$$

The orbital coefficients,  $a_1$  and  $a_2$ , are given by

$$\begin{aligned} a_1 &= \frac{1}{\sqrt{1 + \frac{16t^2}{(U_0 - U_1 + \sqrt{16t^2 + (U_0 - U_1)^2})^2}}}, \\ a_2 &= \frac{1}{\sqrt{2}} \sqrt{\frac{1 + \frac{16t^2}{(U_0 - U_1 + \sqrt{16t^2 + (U_0 - U_1)^2})^2}}{4 + \frac{(U_0 - U_1)^2}{4t^2}}} \approx \frac{1}{\sqrt{2}} \sqrt{\alpha}, \end{aligned}$$

$$\text{where } \alpha \approx \frac{1}{3 + \frac{(U_0 - U_1)^2}{4t^2}} \text{ for } \frac{4t}{(U_0 - U_1)} \ll 1, \quad (12)$$

quantifying the occupation of the left/right symmetrized orbitals and of the doubly occupied orbitals, respectively. Conversely, the coefficient<sup>4</sup>

$$b = \frac{\alpha \mathcal{G}_{\perp} \Im}{\Delta_{\text{SO}}}, \quad (13)$$

quantifies the admixture with higher energy spin and valley states induced by the short-range intervalley scattering. This

<sup>3</sup>To arrive at this simple analytical expression, we assume  $A = X = P \approx 0$ , which is justified for the system under consideration, see Fig. 4, and describes the numerical data well.

<sup>4</sup>This expression Eq. (13) has been derived in first order perturbation theory for  $\hat{Y}$  treating the short-range interactions as a perturbation and assuming nondegenerate levels. This expression hence only holds for  $\Delta_{\text{SO}} \neq 0$ .

short-range interaction  $\propto \mathcal{G}_\perp$  couples different valleys when electrons doubly occupy a site ( $\propto \alpha$ ) for states of the same spin (states  $|S_1\rangle$  and  $|S_6\rangle$ ). Note that all other short-range interaction contributions do not couple different valley states and therefore only lead to shifts in energy  $\propto \mathcal{G}_{zz,0z,z0}$  without inducing mixing between different states. Lastly,

$$C = \sqrt{1 + b^2} \quad (14)$$

ensures normalization.

The states with the orbitally antisymmetric wave function [36],

$$|\Psi_{AS}\rangle = \frac{1}{\sqrt{2}}[|l\rangle|r\rangle - |r\rangle|l\rangle], \quad (15)$$

comprise the multiplet,

$$\begin{aligned} |AS1\rangle &= \frac{|\Psi_{AS}\rangle}{\sqrt{2}}[|- \downarrow\rangle|+ \uparrow\rangle + |+ \uparrow\rangle|- \downarrow\rangle], \\ |AS2\rangle &= |\Psi_{AS}\rangle|- \downarrow\rangle|- \downarrow\rangle, \\ |AS3\rangle &= |\Psi_{AS}\rangle|+ \uparrow\rangle|+ \uparrow\rangle, \\ |AS4\rangle &= \frac{|\Psi_{AS}\rangle}{\sqrt{2}}[|- \downarrow\rangle|- \uparrow\rangle + |- \uparrow\rangle|- \downarrow\rangle], \\ |AS5\rangle &= \frac{|\Psi_{AS}\rangle}{\sqrt{2}}[|- \uparrow\rangle|+ \uparrow\rangle + |+ \uparrow\rangle|- \uparrow\rangle], \\ |AS6\rangle &= \frac{|\Psi_{AS}\rangle}{\sqrt{2}}[|+ \downarrow\rangle|- \downarrow\rangle + |- \downarrow\rangle|+ \downarrow\rangle], \\ |AS7\rangle &= \frac{|\Psi_{AS}\rangle}{\sqrt{2}}[|+ \uparrow\rangle|+ \downarrow\rangle + |+ \downarrow\rangle|+ \uparrow\rangle], \\ |AS8\rangle &= \frac{|\Psi_{AS}\rangle}{\sqrt{2}}[- \uparrow\rangle|+ \downarrow\rangle + |+ \downarrow\rangle|- \uparrow\rangle], \\ |AS9\rangle &= |\Psi_{AS}\rangle|- \uparrow\rangle|- \uparrow\rangle, \\ |AS10\rangle &= |\Psi_{AS}\rangle|+ \downarrow\rangle|+ \downarrow\rangle. \end{aligned} \quad (16)$$

We relate the orbitally symmetric and antisymmetric spin and valley multiplets to product states of spin/valley singlet and triplet states in Appendix B.

We demonstrate the regimes of possible level orderings in Fig. 2 and provide explicit numerical results in for their dependence on dot size, gap size, and interdot distance in representative parameter regimes in Fig. 3. The states with symmetric orbital wave function, Eq. (10), generally yield the lowest-energy states, separated from orbitally antisymmetric states of Eq. (16) by a splitting  $\sim \Delta_{\text{orb}} - \alpha \Im \mathcal{G}_{zz}$ , dominated by the orbital splitting [36]

$$\Delta_{\text{orb}} \approx -\frac{U_0 - U_1}{2} + \frac{1}{2}\sqrt{(U_0 - U_1)^2 + 16t^2}. \quad (17)$$

Within each multiplet, the spin-orbit splitting  $\Delta_{\text{SO}}$  dominates the splittings between different spin and valley states. Additionally, due to the finite weight of doubly occupied sites for states with a symmetric orbital wave function, cf. Eq. (10), the short-range interactions of Eq. (6) induce an additional shift ( $\propto \mathcal{G}_{zz}$ ) and splittings ( $\propto \mathcal{G}_{0z}, \mathcal{G}_{z0}, \mathcal{G}_\perp$ ) of the orbitally

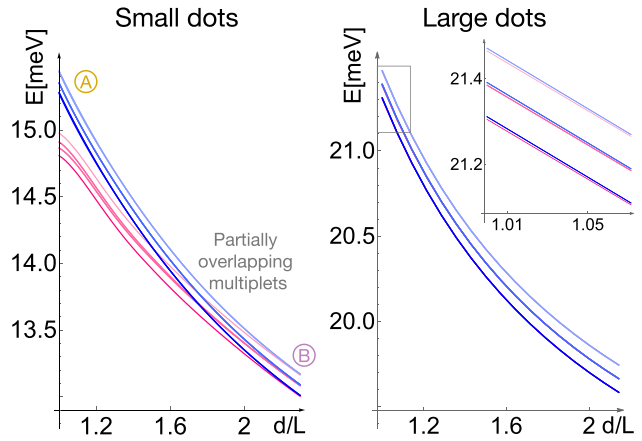


FIG. 3. The two-particle spectra for small dots and small gaps (left,  $L = 30$  nm,  $\Delta_0 = 60$  meV) and large dots and gaps (right,  $L = 70$  nm,  $\Delta_0 = 80$  meV) as a function of interdot separation demonstrate the different regimes for the state orderings,  $\textcircled{A}$  and  $\textcircled{B}$  and the state splittings as discussed in Fig. 2. Here, the dots are oriented along the  $x$  axis and we assume realistic values for the couplings and the spin-orbit splittings,  $\Im \mathcal{G}_\perp \approx 0.075$  meV,  $\mathcal{G}_{0z} \approx \mathcal{G}_{z0} \approx \frac{2}{3} \mathcal{G}_\perp$ ,  $\mathcal{G}_{zz} \approx 10 \mathcal{G}_\perp$ , and  $\Delta_{\text{SO}} \approx -0.04$  meV. We provide spectra for different interaction strengths in Appendix C.

symmetric multiplet. These short-range-induced shifts are proportional to the fraction of double occupation  $\alpha$  and the short-range coupling constants  $\mathcal{G}_{\perp,zz,0z,z0}$ .

The smaller the dots, the gaps, and the interdot distances, the larger the orbital splittings, Eq. (17), and the short-range induced splittings. Hence, in this regime of small and nearby dots ( $\textcircled{A}$  in Figs. 2 and 3), the multiplets of different orbital symmetry are well separated and the ground state is given by an orbitally symmetric state with vanishing total spin and valley pseudospin uniquely selected by the spin-orbit splitting (state  $|S_1\rangle$  in Eq. (10), cf. Fig. 2). In the opposite limit, for large dots, gaps, and separation between the dots ( $\textcircled{B}$  in Figs. 2 and 3), the orbital splitting, Eq. (17), and the short-range induced splittings [ $\propto \alpha$  in Eq. (12)] vanish and the multiplets collapse such that the ground state is fourfold degenerate with orbitally symmetric and antisymmetric states at the same energy, see Figs. 2 and 3.

We demonstrate these different regimes of separated ( $\textcircled{A}$ ) or collapsed ( $\textcircled{B}$ ) multiplets induced by the interplay of the splittings in Fig. 3, where we compare numerical spectra for small double dots and for large double dots as a function of the interdot distance,  $d$ .

We can relate the parameter dependence of the orbital splitting,  $\Delta_{\text{orb}}$  in Eq. (17), and the weight of double occupation,  $\alpha$  in Eq. (12) (determining the short-range splittings), to the Hubbard parameters, Eqs. (8) and (9). Figure 4 exemplifies the dominant Hubbard parameters  $t$ ,  $U_1$ , and  $A$  for different dot and gap sizes and dot orientations. We find nonlocal parameters of an extended Hubbard model to be sizable over a large range of system parameters: For small dots, gaps, and interdot distances both the hopping and the extended Hubbard parameters manifest compared to the onsite Hubbard  $U_0$ . The fast decay of the hopping and the density induced

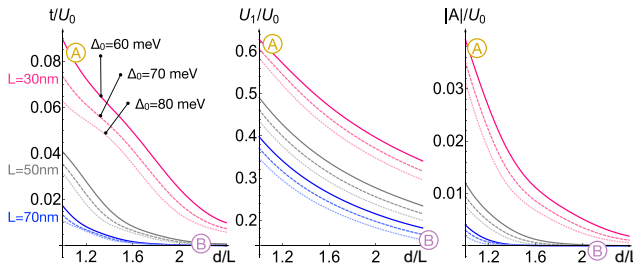


FIG. 4. Hubbard parameters (single-particle hopping  $t$ , nearest-neighbor direct interaction  $U_1$ , and density-assisted hopping  $A$ ) for different dot diameters  $L$  and ga  $\Delta_0$  as a function of the interdot distance  $d$ . Interdot interaction processes are sizable compared to the on-site interaction  $U_0$  over an extensive range of system parameters, making the description of BLG multidots in terms of an extended Hubbard model necessary. The labels Ⓢ and Ⓣ refer to the different regimes of two-particle level schemes in Fig. 2. Here, the dots are oriented along the  $x$  axis, we provide similar data for dots oriented along the  $y$  axis in Appendix C.

tunneling with  $d$  leaves the direct interaction as the dominant nonlocal Hubbard parameter at larger interdot distances. Conversely, we found the exchange parameters  $X$  and the pairwise hopping parameters  $P$  to be negligibly small compared to the other Hubbard terms (we show the data for all parameters explicitly in Appendix C).

### III. DOUBLE DOT IN A MAGNETIC FIELD: EFFECTIVE SPIN HEISENBERG MODEL

A perpendicular magnetic field splits the spin and the valley states, respectively, according to their  $g$  factors,  $g_s$  and  $g_v$ . Hence, at finite  $B$ , the single-particle wave function changes due to this shift in energy within a soft confinement potential whose radius changes with energy, the compression by the magnetic field, and the  $B$ -dependent phase factor in the single-particle wave functions  $\varphi_{l/r}(\mathbf{r})$  of the individual dots. These  $B$ -dependent effects combined entail a nonmonotonic dependence of the Hubbard parameters on the magnetic field strength as we demonstrate in Fig. 5.

We find that these orbital magnetic field effects are small compared to the field induced valley splitting, see Fig. 5, right panel. The valley  $g$  factor (induced by the topological orbital magnetic moment of the BLG Bloch bands) can be orders of magnitude larger than the spin  $g$  factor [5,12,21,22,100,101,120] and hence valley Zeeman splitting dominates the single-particle level ordering at finite magnetic field.

Due to this prevalence of the field-induced valley splitting, the double dot's low-energy multiplet in a finite magnetic field consists of the valley polarized two-particle states. By projecting onto the well-separated valley polarized states, we describe the low-energy multiplet by an effective Heisenberg model for the spins, [41],

$$\hat{H}_{\text{eff},B} = E_V + \mathcal{J}_{\text{eff}} \mathbf{S}_l \cdot \mathbf{S}_r + \mu_B \mathcal{B}_{\text{eff}} (S_l^z + S_r^z), \quad (18)$$

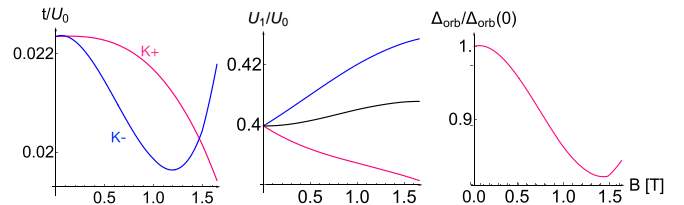


FIG. 5. Extended Hubbard parameters (tunnelling  $t$  and nearest-neighbor direct interaction  $U_1$ ) and the orbital splitting  $\Delta_{\text{orb}}$  as a function of magnetic field  $B$  for  $L = 50\text{ nm}$ ,  $\Delta_0 = 70\text{ meV}$ , and  $d = 1.2L$  for two dots aligned along the  $x$  axis. Magenta/blue/black lines represent processes involving states in the  $K^+/K^-$ /either valley. Changes in the orbital splitting due to these field-induced modulations of the Hubbard parameters are weak compared to the overall splitting scale (rightmost panel). We provide the corresponding data for dots oriented along the  $y$  axis in Appendix C.

where

$$E_V = g_v \mu_B B, \quad (19)$$

is the global energy of the valley polarized multiplet and

$$\begin{aligned} \mathcal{J}_{\text{eff}} &= \Delta_{\text{orb}} - \alpha 2\Im \left( \mathcal{G}_{0z} + \mathcal{G}_{z0} + \frac{1}{2} \mathcal{G}_{zz} \right), \\ \mathcal{B}_{\text{eff}} &= 2 \frac{\Delta_{\text{SO}}}{\mu_B} + g_s B, \end{aligned} \quad (20)$$

represent an effective exchange coupling and an effective magnetic field capturing the combined effect of the external magnetic field  $B$  and the material's characteristics.

We examine the effective Heisenberg model of Eq. (18) describing the four valley polarized low-energy spin singlet and triplet states in Fig. 6. In the effective magnetic field  $\mathcal{B}_{\text{eff}}$ , Eq. (20), the Zeeman coupling and the spin-orbit gap compete. This competition entails different level orderings depending on the signs and strengths of  $\Delta_{\text{SO}}$  and  $\mu_B B$ , as demonstrated in the top panels of Fig. 6 for a positive magnetic field which singles out the  $K^+$  polarized multiplet in our convention. The spin-orbit and the Zeeman effect favoring different spin and valley states (here, this is the case for  $\Delta_{\text{SO}} < 0$ ), leads to a reversal of the order within the orbitally antisymmetric states at a critical field strength, see Fig. 6(a). Conversely, when  $\Delta_{\text{SO}}$  and  $\mu_B B$  favour the same spin and valley state (here,  $\Delta_{\text{SO}} > 0$ ), no such state reordering occurs, cf. Fig. 6(b). For sufficiently large field strengths, the valley and spin-polarized state favoured by the Zeeman coupling becomes the global ground state in either case. A negative magnetic field entails the corresponding level schemes in the  $K^-$  polarized multiplet. We show the orderings of all the states in Appendix D.

For the effective exchange constant  $\mathcal{J}_{\text{eff}}$ , Eq. (20), the contributions from orbital and short-range interactions compete. A dominant orbital splitting,  $\Delta_{\text{orb}}$ , entails  $\mathcal{J}_{\text{eff}} > 0$ . Conversely, sufficiently strong screening of the orbital contributions, such that  $|U_0 - U_1| < 2\Im(\mathcal{G}_{0z} + \mathcal{G}_{z0} + \frac{1}{2}\mathcal{G}_{zz})$ , allows

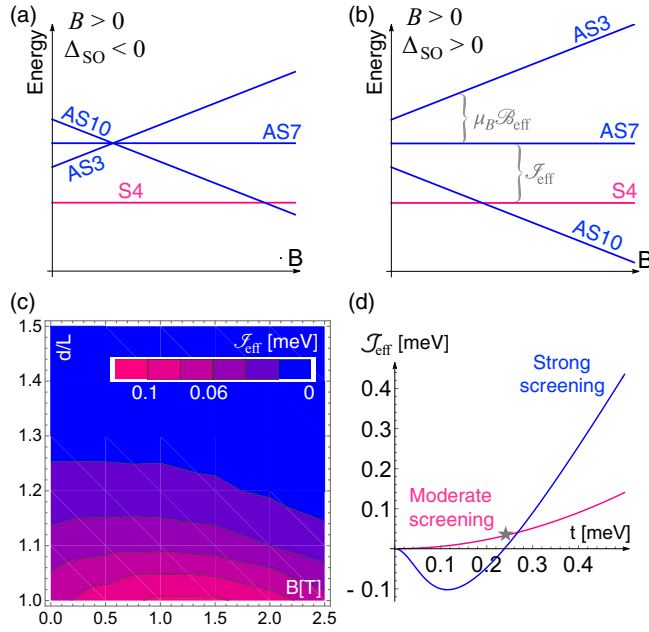


FIG. 6. (Top) Level orderings in the low-energy valley polarized multiplet at finite magnetic field  $B > 0$  described by the effective anisotropic Heisenberg model, Eq. (18) for different sign of the spin-orbit-splitting,  $\Delta_{SO} < 0$  (a) or  $\Delta_{SO} > 0$  (b). For clarity, we omitted the global energy shift,  $E_V$ , of the valley polarized multiplet and the explicit dependence of  $J_{\text{eff}}$  on  $B$ . (Bottom) Effective exchange constant,  $J_{\text{eff}}$ , as a function of parameters. (c)  $J_{\text{eff}}$  as a function of magnetic field  $B$  and interdot distance  $d$  evaluated from the data in Fig. 5. (d)  $J_{\text{eff}}$  as a function of the hopping  $t$  assuming the screening of extended Hubbard parameters to be of different strengths. The magenta line is obtained using  $U_0$  and  $U_1$  for the parameters in Fig. 5 (the star marking the corresponding value of  $t$ ). The blue line assumes  $U_0$  and  $U_1$  to be reduced by a factor of 10, allowing for negative values as the orbital interactions become comparable to the short-range interactions.

for negative values of  $J_{\text{eff}}$  for small hoppings  $t$ , as we demonstrate in the right panel of Fig. 6. Being able to control the effective exchange constant would be useful in a scenario using such double dots, e.g., as two-qubit gates [36,134,135]. Further, the possibility to control  $J_{\text{eff}}$  via multiple parameters (such as screening, interdot distance, magnetic field, and the gates) will provide enhanced sensitivity against noise [34,136]. We discuss possible ways to tune the different parameters experimentally in the conclusion.

#### IV. CONCLUSIONS AND OUTLOOK

We set up and parametrized a Hubbard model for interacting QDs in BLG and studied a double QD as the smallest possible example. We characterized the low-energy two-particle multiplets of the double dot in terms of their orbital, spin, and valley configuration and study their dependence on the system parameters and an external magnetic field. The various spin and valley phases are driven by the interplay of extended Hubbard parameters induced by

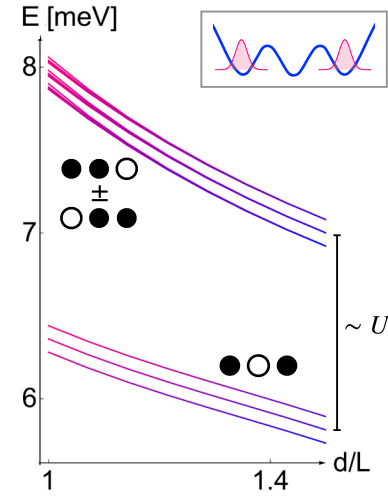


FIG. 7. Spectrum of two interacting electrons in a triple dot chain oriented along the  $x$  axis, described by a Hubbard model with the extended Hubbard parameters in Fig. 4 for  $L = 70$  nm and  $\Delta = 60$  meV, plotted as a function of the interdot distance  $d$ . The ground state multiplet consists of the same spin and valley states as the double dot, where the electrons prefer to sit in the outermost sites in order to minimize their energy. Only the excited states' multiplet allows for two electrons to reside in adjacent dots. The separation between the ground and excited states' multiplets is of the order of the nearest-neighbor direct interaction,  $U_1$ .

long-range Coulomb interaction and short-range interactions on the lattice scale.

This competition of interactions on different scales opens ample ways to manipulate and tune the dot states and the couplings. We discuss the dependence of the states and splittings on the dot size and separation, affecting the orbital wave function and the tunneling, cf. Figs. 3, 4, and 6.

In future work, one may explore, e.g., dot state tuning by deformation of the QDs into ellipses and by an independently adjustable tunneling barrier (the former can be achieved by having split gates and finger gates of different dimensions, the latter by adding an additional finger gate in between the two QDs) [9,17,27,29]. Further, we expect the long-range interactions to be strongly affected by environmental screening as opposed to short-range interactions largely confined to the BLG lattice. This difference in screening response may allow for efficient dielectric engineering of the different interaction parameters [137–139].

We note that the nonlocal Hubbard parameters for the BLG double dot (the nearest-neighbor direct interaction,  $U_1$ , in particular) remain finite over an extensive range of system parameters, including the interdot separation, cf. Fig. 4. Therefore one indeed requires an extended Hubbard model framework to describe a BLG multidot system faithfully. Long-range extended Hubbard parameters will also affect lattices with more than two dots over several dot sites, as we demonstrate for a triple QD in Fig. 7. Here, the two-particle ground state preferring to maximize the distance between the electrons is driven by interdot interactions, in particular the nearest-neighbor direct interaction  $U_1$ . In future

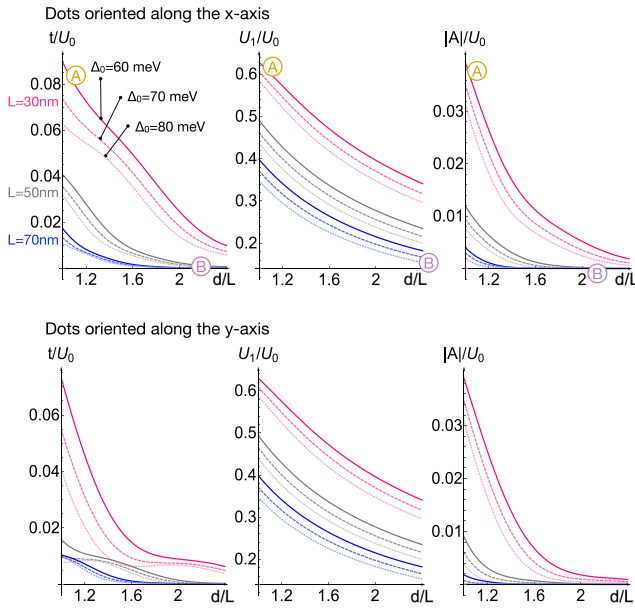


FIG. 8. Hubbard parameters as a function of the interdot separation  $d$  for dots oriented along the  $x$  axis (top) or along the  $y$  axis (bottom). There is little difference for the extended Hubbard parameters,  $U_1$  and  $A$ , while the single-particle hopping is slightly reduced for dots aligned along the  $y$  axis (cf. Fig. 4 in the main text).

work, one may employ an extended Hubbard model approach as developed in this work, to study BLG QD lattices with larger numbers of dots, where additional intricacies, such as long-range intersite interactions, band overlap, and multi-orbital physics may make for interesting Fermi-Hubbard physics.

Besides the use of the spin and valley degree of freedom for quantum information processing in multiqubit systems, larger dot lattices with tunable long-range and spin and valley-dependent short-range interactions may hence also allow for quantum simulation of exotic Hubbard models using BLG QD lattices.

## ACKNOWLEDGMENTS

We thank Samuel Möller, Katrin Hecker, Christoph Stampfer, Thierry Jolicœur, Oded Zilberberg, Jonathan Brugger, and Dennis Mayer for fruitful discussions. A.K. acknowledges support from the Deutsche Forschungsgemeinschaft (DFG, German Research Foundation) within Project-ID 314695032-SFB 1277 and DFG Individual grant KN 1383/4, Project-ID 529637137.

## APPENDIX A: RELATION OF THE HUBBARD PARAMETERS

We label the four states in each dot with indices  $\{h, j, k, m\} \in \{0, \dots, 7\}$ , relating  $|0\rangle = |l:\uparrow+\rangle$ ,  $|1\rangle = |l:\downarrow+\rangle$ ,  $|2\rangle = |l:\uparrow-\rangle$ ,  $|3\rangle = |l:\downarrow-\rangle$ ,  $|4\rangle = |r:\uparrow+\rangle$ ,  $|5\rangle = |r:\downarrow+\rangle$ ,  $|6\rangle = |r:\uparrow-\rangle$ ,  $|7\rangle = |r:\downarrow-\rangle$ . In this notation, we relate the Hubbard parameters as follows (listing the nonzero matrix elements  $t_{jk}$  with  $k > j$  and  $U_{hjkm}$  with  $j > h$  and  $k > m$ ):

$$t_{04} = t_{15} = t_{26} = t_{37} = t,$$

$$U_{0110} = U_{2332} = U_0 + \mathfrak{J}[\mathcal{G}_{zz} + \mathcal{G}_{z0} + \mathcal{G}_{0z}],$$

$$\begin{aligned} U_{0220} &= U_{0330} = U_{1221} = U_{1331} = U_0 + \mathfrak{J}[\mathcal{G}_{zz} - (\mathcal{G}_{z0} + \mathcal{G}_{0z})], \\ U_{0202} &= U_{0312} = U_{1313} = U_{1203} = 4\mathfrak{J}\mathcal{G}_\perp, \\ U_{0440} &= U_{0550} = U_{0660} = U_{0770} = U_{1441} = U_{1551} = U_{1661} \\ &= U_{1771} = U_{2442} = U_{2552} = U_{2662} = U_{2772} = U_{3443} \\ &= U_{3553} = U_{3663} = U_{3773} = U_1, \\ U_{0404} &= U_{1515} = U_{2626} = U_{3737} = X, \\ U_{0154} &= U_{0264} = U_{0374} = U_{1265} = U_{1375} = U_{2376} = P, \\ U_{1261} &= U_{1371} + U_{2372} = U_{1621} = U_{0150} = U_{0260} = U_{0370} \\ &= U_{0510} = U_{0620} = U_{0730} = U_{1401} = U_{1731} = U_{2732} \\ &= U_{2402} = U_{2512} = U_{3403} = U_{3623} = U_{3513} = A. \end{aligned} \quad (\text{A1})$$

## APPENDIX B: RELATION TO SPIN AND VALLEY TRIPLET STATES

We relate the two-particle states in Eqs. (10) and (16) to the spin and valley triplet states. For this Appendix, we adopt notation commonly used in the literature [132] to denote the spin ( $s$ ) and valley ( $v$ ) singlet ( $|S\rangle$ ) and triplet ( $|T_{-,0,+}\rangle$ ) states as

$$\begin{aligned} |S\rangle^s &= \frac{1}{\sqrt{2}}(|\uparrow\downarrow\rangle - |\downarrow\uparrow\rangle), \\ |T_-\rangle^s &= |\downarrow\downarrow\rangle, \\ |T_0\rangle^s &= \frac{1}{\sqrt{2}}(|\uparrow\downarrow\rangle + |\downarrow\uparrow\rangle), \\ |T_+\rangle^s &= |\uparrow\uparrow\rangle, \\ |S\rangle^v &= \frac{1}{\sqrt{2}}(|+-\rangle - |-+\rangle), \\ |T_-\rangle^v &= |--\rangle, \\ |T_0\rangle^v &= \frac{1}{\sqrt{2}}(|+-\rangle + |-+\rangle), \\ |T_+\rangle^v &= |++\rangle. \end{aligned} \quad (\text{B1})$$

and combinations thereof.

Using the notation above, we relate

$$\begin{aligned} |S1\rangle &= \frac{|\Psi_S\rangle}{C} [(|S\rangle^v|T_0\rangle^s + |T_0\rangle^v|S\rangle^s) \\ &\quad + b(|S\rangle^v|T_0\rangle^s - |T_0\rangle^v|S\rangle^s)], \\ |S2\rangle &= -|\Psi_S\rangle|S\rangle^v|T_-\rangle^s, \\ |S3\rangle &= |\Psi_S\rangle|S\rangle^v|T_+\rangle^s, \\ |S4\rangle &= -|\Psi_S\rangle|T_+\rangle^v|S\rangle^s, \\ |S5\rangle &= |\Psi_S\rangle|T_-\rangle^v|S\rangle^s, \\ |S6\rangle &= \frac{|\Psi_S\rangle}{C} [(|S\rangle^v|T_0\rangle^s - |T_0\rangle^v|S\rangle^s) \\ &\quad + b(|S\rangle^v|T_0\rangle^s + |T_0\rangle^v|S\rangle^s)], \end{aligned} \quad (\text{B2})$$

and

$$\begin{aligned} |AS1\rangle &= |\Psi_{AS}\rangle(|T_0\rangle^v|T_0\rangle^s + |S\rangle^v|S\rangle^s), \\ |AS2\rangle &= |\Psi_{AS}\rangle|T_-\rangle^v|T_-\rangle^s, \end{aligned}$$

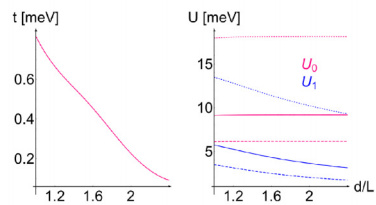
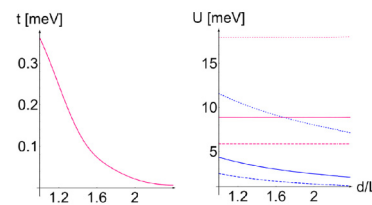
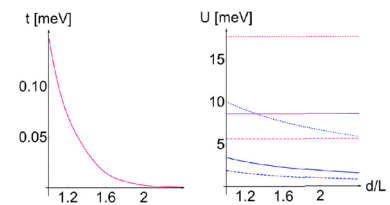
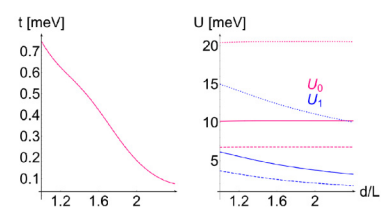
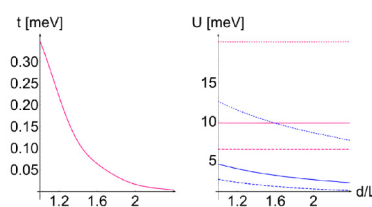
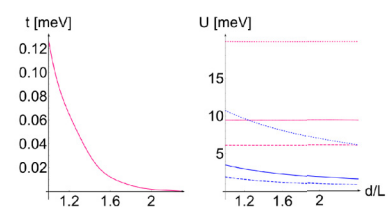
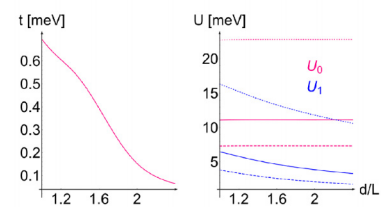
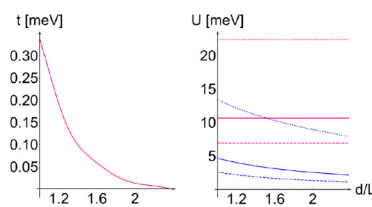
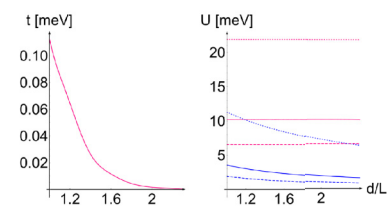
$\Delta_0 = 60 \text{ meV}$  $L = 30 \text{ nm}$  $L = 50 \text{ nm}$  $L = 70 \text{ nm}$  $\Delta_0 = 70 \text{ meV}$  $L = 30 \text{ nm}$  $L = 50 \text{ nm}$  $L = 70 \text{ nm}$  $\Delta_0 = 80 \text{ meV}$  $L = 30 \text{ nm}$  $L = 50 \text{ nm}$  $L = 70 \text{ nm}$ 

FIG. 9. Hubbard parameters  $t$ ,  $U_0$ ,  $U_1$ ,  $P$ ,  $A$ , and  $X$  (cf. Eqs. (8) and (9)) as a function of the interdot separation  $d$  over a large range of system parameters.

Small dots

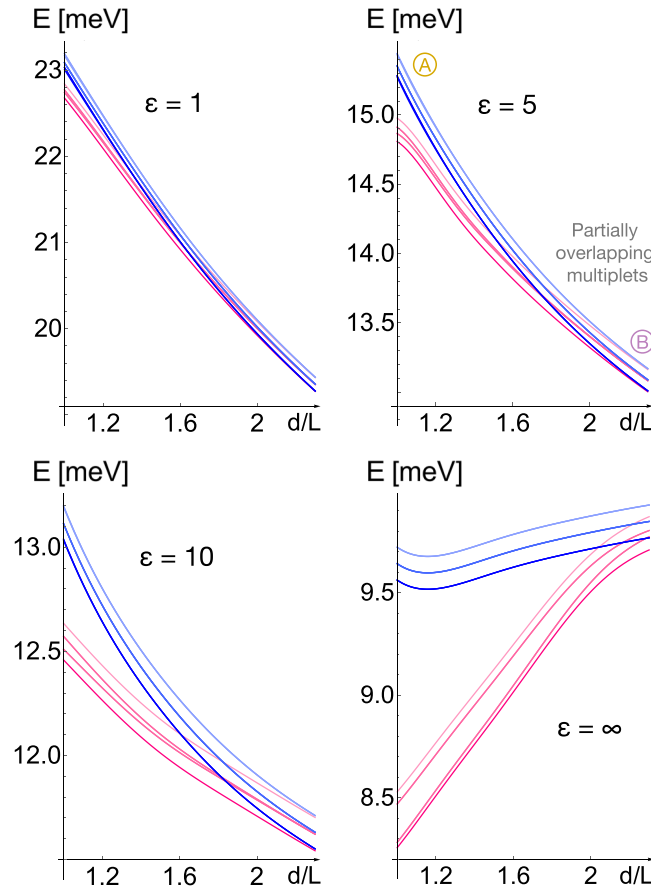


FIG. 10. Same as Fig. 3 in the main text for different values of the dielectric constant  $\epsilon$ . Two-particle spectra for  $L = 30$  nm and  $\Delta_0 = 60$  meV.

$$\begin{aligned} |AS3\rangle &= |\Psi_{AS}\rangle|T_+\rangle^v|T_+\rangle^s, \\ |AS4\rangle &= |\Psi_{AS}\rangle|T_-\rangle^v|T_0\rangle^s, \\ |AS5\rangle &= |\Psi_{AS}\rangle|T_0\rangle^v|T_+\rangle^s, \\ |AS6\rangle &= |\Psi_{AS}\rangle|T_0\rangle^v|T_-\rangle^s, \\ |AS7\rangle &= |\Psi_{AS}\rangle|T_+\rangle^v|T_0\rangle^s, \\ |AS8\rangle &= |\Psi_{AS}\rangle(|T_0\rangle^v|T_0\rangle^s - |S\rangle^v|S\rangle^s), \\ |AS9\rangle &= |\Psi_{AS}\rangle|T_-\rangle^v|T_+\rangle^s, \\ |AS10\rangle &= |\Psi_{AS}\rangle|T_+\rangle^v|T_-\rangle^s. \end{aligned} \quad (B3)$$

### APPENDIX C: EXTENDED DATA FOR THE HUBBARD PARAMETERS

In this Appendix, we provide numerical data for the Hubbard parameters in Eqs. (8) and (9) as well as for the two-particle spectra over a larger parameter range compared to the main text. Figure 8 compares the hopping  $t$ , next-neighbor direct interaction  $U_1$ , and the density assisted hopping  $A$  for the scenarios where the two dots are aligned along the  $x$  axis or the  $y$  axis. The breaking of rotational symmetry in BLG translates into the single-particle wave functions and hence the Hubbard parameters. Nevertheless, we observe in Fig. 8

Large dots

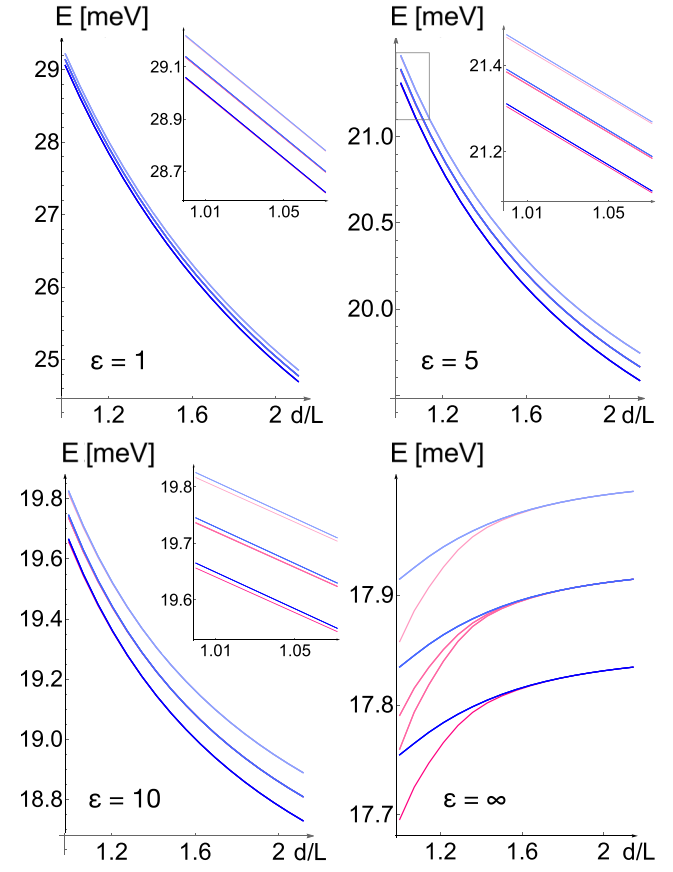


FIG. 11. Same as Fig. 3 in the main text for different values of the dielectric constant,  $\epsilon$ . Two-particle spectra for  $L = 70$  nm and  $\Delta_0 = 80$  meV.

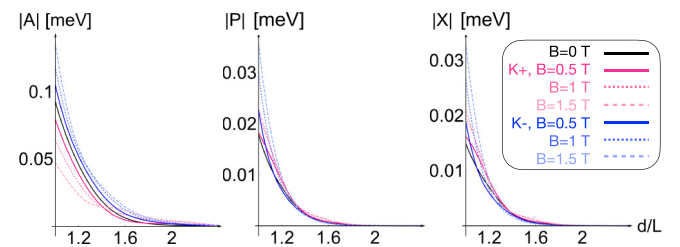
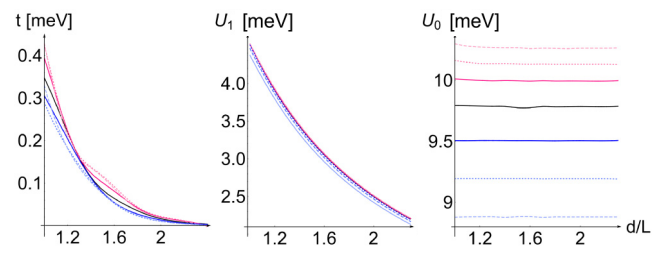


FIG. 12. Hubbard parameters as a function of the interdot separation,  $d$ , for  $\Delta_0 = 70$  meV and  $L = 50$  nm in the  $K^+$  valley (magenta) and  $K^-$  valley (blue) for different  $B$ .

that the parameters are of similar order of magnitude for both orientations (mostly the hopping  $t$  is slightly reduced for orientations along the  $y$  axis as compared to the  $x$  axis). We hence conclude all qualitative statements from the main text to be valid independent of the orientation of the QD chain with respect to the lattice.

Further, Fig. 9 provides the unnormalized Hubbard parameters for two dots oriented along the  $x$  axis over an extensive parameter range. We vary the gap  $\Delta_0$ , the dot diameter  $L$ , the interdot separation  $d$ , and the dielectric constant  $\epsilon$  of the encapsulating medium.

Finally, Figs. 10 and 11 illustrate the dependence of the low-energy two-particle multiplets on the interaction strength tuned by the dielectric constant,  $\epsilon$  (cf. Fig. 3 in the main text). Increasing the screening decreases the Hubbard parameters induced by the long-range Coulomb interactions, cf. Fig. 9. The splitting between the orbitally symmetric and antisymmetric multiplet decreases with increasing interaction strength at fixed tunneling (i.e., fixed interdot distance) as predicted by the dependence of the orbital splitting  $\Delta_{\text{orb}}$ , Eq. (17), on the Hubbard parameters. At low screening, there is an interplay between the long-range and short-range interactions and the tunneling. For sufficiently large screening, the splittings are governed by  $t$ , and the short-range interactions.

#### APPENDIX D: DOUBLE DOT IN A MAGNETIC FIELD

In this Appendix, we provide additional information concerning the BLGdouble-QD in an external perpendicular magnetic field.

Figure 12 demonstrates the nonmonotonic dependence of the Hubbard parameters  $t$ ,  $U_0$ ,  $U_1$ ,  $P$ ,  $A$ , and  $X$  in the  $K^+$  and  $K^-$  valley on the magnetic field strength (cf. Fig. 5 in the main text).

Figure 13 illustrates the level ordering of all two-particle double dot states, Eqs. (10) and (16), in a finite magnetic field  $B > 0$  depending on the sign of the spin-orbit-coupling gap and the external magnetic field strength for the parameters chosen in the main text.

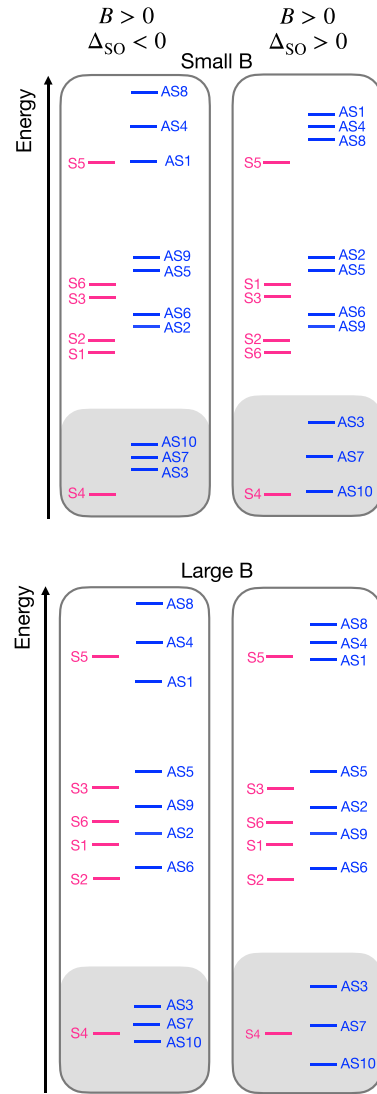


FIG. 13. Level ordering of the two-particle double dot states in a finite magnetic field  $B > 0$  depending on the sign of the spin-orbit-coupling gap and the external magnetic field strength. The gray shade highlights the  $K^+$  valley-polarized low-energy states we focus on in the main text.

- [1] M. Eich, F. Herman, R. Pisoni, H. Overweg, A. Kurzmann, Y. Lee, P. Rickhaus, K. Watanabe, T. Taniguchi, M. Sigrist, T. Ihn, and K. Ensslin, Spin and valley states in gate-defined bilayer graphene quantum dots, *Phys. Rev. X* **8**, 031023 (2018).
- [2] L. Banszerus, B. Frohn, A. Epping, D. Neumaier, K. Watanabe, T. Taniguchi, and C. Stampfer, Gate-defined electron–hole double dots in bilayer graphene, *Nano Lett.* **18**, 4785 (2018).
- [3] R. Garreis, J. D. Gerber, V. Stará, C. Tong, C. Gold, M. Röösli, K. Watanabe, T. Taniguchi, K. Ensslin, T. Ihn, and A. Kurzmann, Counting statistics of single electron transport in bilayer graphene quantum dots, *Phys. Rev. Res.* **5**, 013042 (2023).
- [4] R. Garreis, A. Knothe, C. Tong, M. Eich, C. Gold, K. Watanabe, T. Taniguchi, V. Fal’ko, T. Ihn, K. Ensslin, and A. Kurzmann, Shell filling and trigonal warping in graphene quantum dots, *Phys. Rev. Lett.* **126**, 147703 (2021).
- [5] C. Tong, R. Garreis, A. Knothe, M. Eich, A. Sacchi, K. Watanabe, T. Taniguchi, V. Fal’ko, T. Ihn, K. Ensslin, and A. Kurzmann, Tunable valley splitting and bipolar operation in graphene quantum dots, *Nano Lett.* **21**, 1068 (2021).
- [6] A. Kurzmann, Y. Kleeorin, C. Tong, R. Garreis, A. Knothe, M. Eich, C. Mittag, C. Gold, F. K. de Vries, K. Watanabe, T. Taniguchi, V. Fal’ko, Y. Meir, T. Ihn, and K. Ensslin, Kondo effect and spin–orbit coupling in graphene quantum dots, *Nat. Commun.* **12**, 6004 (2021).
- [7] L. M. Gächter, R. Garreis, J. D. Gerber, M. J. Ruckriegel, C. Tong, B. Kratochwil, F. K. de Vries, A. Kurzmann, K. Watanabe, T. Taniguchi, T. Ihn, K. Ensslin, and W. W. Huang,

- Single-shot spin readout in graphene quantum dots, *PRX Quantum* **3**, 020343 (2022).
- [8] L. Banszerus, S. Möller, E. Icking, C. Steiner, D. Neumaier, M. Otto, K. Watanabe, T. Taniguchi, C. Volk, and C. Stampfer, Dispersive sensing of charge states in a bilayer graphene quantum dot, *Appl. Phys. Lett.* **118**, 093104 (2021).
- [9] L. Banszerus, A. Rothstein, T. Fabian, S. Möller, E. Icking, S. Trellenkamp, F. Lentz, D. Neumaier, K. Watanabe, T. Taniguchi, F. Libisch, C. Volk, and C. Stampfer, Electron-hole crossover in gate-controlled bilayer graphene quantum dots, *Nano Lett.* **20**, 7709 (2020).
- [10] S. Möller, L. Banszerus, A. Knothe, L. Valerius, K. Hecker, E. Icking, K. Watanabe, T. Taniguchi, C. Volk, and C. Stampfer, Impact of competing energy scales on the shell-filling sequence in elliptic bilayer graphene quantum dots, *Phys. Rev. B* **108**, 125128 (2023).
- [11] L. Banszerus, S. Möller, K. Hecker, E. Icking, K. Watanabe, T. Taniguchi, F. Hassler, C. Volk, and C. Stampfer, Particle-hole symmetry protects spin-valley blockade in graphene quantum dots, *Nature (London)* **618**, 51 (2023).
- [12] S. Möller, L. Banszerus, A. Knothe, C. Steiner, E. Icking, S. Trellenkamp, F. Lentz, K. Watanabe, T. Taniguchi, L. I. Glazman, V. I. Fal'ko, C. Volk, and C. Stampfer, Probing two-electron multiplets in bilayer graphene quantum dots, *Phys. Rev. Lett.* **127**, 256802 (2021).
- [13] L. Banszerus, K. Hecker, E. Icking, S. Trellenkamp, F. Lentz, D. Neumaier, K. Watanabe, T. Taniguchi, C. Volk, and C. Stampfer, Pulsed-gate spectroscopy of single-electron spin states in bilayer graphene quantum dots, *Phys. Rev. B* **103**, L081404 (2021).
- [14] L. Banszerus, K. Hecker, S. Möller, E. Icking, K. Watanabe, T. Taniguchi, C. Volk, and C. Stampfer, Spin relaxation in a single-electron graphene quantum dot, *Nat. Commun.* **13**, 3637 (2022).
- [15] L. Banszerus, S. Möller, C. Steiner, E. Icking, S. Trellenkamp, F. Lentz, K. Watanabe, T. Taniguchi, C. Volk, and C. Stampfer, Spin-valley coupling in single-electron bilayer graphene quantum dots, *Nat. Commun.* **12**, 5250 (2021).
- [16] Y.-N. Ren, Q. Cheng, Q.-F. Sun, and L. He, Realizing valley-polarized energy spectra in bilayer graphene quantum dots via continuously tunable berry phases, *Phys. Rev. Lett.* **128**, 206805 (2022).
- [17] L. Banszerus, A. Rothstein, E. Icking, S. Möller, K. Watanabe, T. Taniguchi, C. Stampfer, and C. Volk, Tunable interdot coupling in few-electron bilayer graphene double quantum dots, *Appl. Phys. Lett.* **118**, 103101 (2021).
- [18] F.-M. Jing, G.-Q. Qin, Z.-Z. Zhang, X.-X. Song, and G.-P. Guo, Tunable p-n junction barriers in few-electron bilayer graphene quantum dots, *Appl. Phys. Lett.* **123**, 184001 (2023).
- [19] H. Duprez, S. Cances, A. Omahen, M. Masseroni, M. J. Ruckriegel, C. Adam, C. Tong, J. Gerber, R. Garreis, W. Huang, L. Gächter, T. Taniguchi, K. Watanabe, T. Ihn, and K. Ensslin, Spectroscopy of a single-carrier bilayer graphene quantum dot from time-resolved charge detection, *arXiv:2311.12949* [cond-mat.mes-hall].
- [20] R. Garreis, C. Tong, J. Terle, M. J. Ruckriegel, J. D. Gerber, L. M. Gächter, K. Watanabe, T. Taniguchi, T. Ihn, K. Ensslin, and W. W. Huang, Long-lived valley states in bilayer graphene quantum dots, *Nature Phys.* **20**, 428 (2024).
- [21] A. Knothe and V. Fal'ko, Quartet states in two-electron quantum dots in bilayer graphene, *Phys. Rev. B* **101**, 235423 (2020).
- [22] D. Mayer and A. Knothe, Tuning-confined states and valley G-factors by quantum dot design in bilayer graphene, *Phys. Status Solidi (B)* **260**, 2300395 (2023).
- [23] A. Knothe, L. I. Glazman, and V. I. Fal'ko, Tunneling theory for a bilayer graphene quantum dot's single- and two-electron states, *New J. Phys.* **24**, 043003 (2022).
- [24] S. Schnez, K. Ensslin, M. Sigrist, and T. Ihn, Analytic model of the energy spectrum of a graphene quantum dot in a perpendicular magnetic field, *Phys. Rev. B* **78**, 195427 (2008).
- [25] P. Recher, J. Nilsson, G. Burkard, and B. Trauzettel, Bound states and magnetic field induced valley splitting in gate-tunable graphene quantum dots, *Phys. Rev. B* **79**, 085407 (2009).
- [26] M. Eich, R. Pisoni, A. Pally, H. Overweg, A. Kurzmann, Y. Lee, P. Rickhaus, K. Watanabe, T. Taniguchi, K. Ensslin, and T. Ihn, Coupled quantum dots in bilayer graphene, *Nano Lett.* **18**, 5042 (2018).
- [27] C. Tong, A. Kurzmann, R. Garreis, K. Watanabe, T. Taniguchi, T. Ihn, and K. Ensslin, Pauli blockade catalogue in bilayer graphene double quantum dots, *Phys. Rev. Res.* **6**, L012006 (2024).
- [28] K. Hecker, L. Banszerus, A. Schäpers, S. Möller, A. Peters, E. Icking, K. Watanabe, T. Taniguchi, C. Volk, and C. Stampfer, Coherent charge oscillations in a bilayer graphene double quantum dot, *Nat. Commun.* **14**, 7911 (2023).
- [29] C. Tong, F. Ginzel, W. W. Huang, A. Kurzmann, R. Garreis, K. Watanabe, T. Taniguchi, G. Burkard, J. Danon, T. Ihn, and K. Ensslin, Three-carrier spin blockade and coupling in bilayer graphene double quantum dots, *arXiv:2211.04882* [cond-mat.mes-hall].
- [30] L. Banszerus, S. Möller, E. Icking, K. Watanabe, T. Taniguchi, C. Volk, and C. Stampfer, Single-electron double quantum dots in bilayer graphene, *Nano Lett.* **20**, 2005 (2020).
- [31] C. Tong, A. Kurzmann, R. Garreis, W. W. Huang, S. Jele, M. Eich, L. Ginzburg, C. Mittag, K. Watanabe, T. Taniguchi, K. Ensslin, and T. Ihn, Pauli blockade of tunable two-electron spin and valley states in graphene quantum dots, *Phys. Rev. Lett.* **128**, 067702 (2022).
- [32] N. Rohling and G. Burkard, Universal quantum computing with spin and valley states, *New J. Phys.* **14**, 083008 (2012).
- [33] J. R. Schaibley, H. Yu, G. Clark, P. Rivera, J. S. Ross, K. L. Seyler, W. Yao, and X. Xu, Valleytronics in 2D materials, *Nat. Rev. Mater.* **1**, 16055 (2016).
- [34] G. Burkard, T. D. Ladd, A. Pan, J. M. Nichol, and J. R. Petta, Semiconductor spin qubits, *Rev. Mod. Phys.* **95**, 025003 (2023).
- [35] D. Loss and D. P. DiVincenzo, Quantum computation with quantum dots, *Phys. Rev. A* **57**, 120 (1998).
- [36] G. Burkard, D. Loss, and D. P. DiVincenzo, Coupled quantum dots as quantum gates, *Phys. Rev. B* **59**, 2070 (1999).
- [37] D. Fernández-Fernández, Y. Ban, and G. Platero, Quantum control of hole spin qubits in double quantum dots, *Phys. Rev. Appl.* **18**, 054090 (2022).
- [38] M. Brooks and C. Tahan, Hybrid exchange-measurement-based qubit operations in semiconductor double-quantum-dot qubits, *Phys. Rev. Appl.* **16**, 064019 (2021).

- [39] I. Heinz and G. Burkard, Crosstalk analysis for simultaneously driven two-qubit gates in spin qubit arrays, *Phys. Rev. B* **105**, 085414 (2022).
- [40] H. Goto, Y. Ho, and T. Kanao, Measurement-free fault-tolerant logical-zero-state encoding of the distance-three nine-qubit surface code in a one-dimensional qubit array, *Phys. Rev. Res.* **5**, 043137 (2023).
- [41] N. Read and S. Sachdev, Some features of the phase diagram of the square lattice SU(N) antiferromagnet, *Nucl. Phys. B* **316**, 609 (1989).
- [42] K. Tamura and H. Katsura, Ferromagnetism in d-dimensional SU(n) Hubbard models with nearly flat bands, *J. Stat. Phys.* **182**, 16 (2021).
- [43] R. Samajdar and R. N. Bhatt, Polaronic mechanism of nagaoka ferromagnetism in Hubbard models, [arXiv:2311.09279](#) [cond-mat.str-el].
- [44] J. Willsher, H.-K. Jin, and J. Knolle, Magnetic excitations, phase diagram, and order-by-disorder in the extended triangular-lattice Hubbard model, *Phys. Rev. B* **107**, 064425 (2023).
- [45] Y. Yu, S. Li, S. Iskakov, and E. Gull, Magnetic phases of the anisotropic triangular lattice Hubbard model, *Phys. Rev. B* **107**, 075106 (2023).
- [46] J. P. Dehollain, U. Mukhopadhyay, V. P. Michal, Y. Wang, B. Wunsch, C. Reichl, W. Wegscheider, M. S. Rudner, E. Demler, and L. M. K. Vandersypen, Nagaoka ferromagnetism observed in a quantum dot plaquette, *Nature (London)* **579**, 528 (2020).
- [47] R. Samajdar and R. N. Bhatt, Nagaoka ferromagnetism in doped Hubbard models in optical lattices, [arXiv:2305.05683](#) [cond-mat.str-el].
- [48] P. R. Bas and A. A. Aligia, Phase diagram of the ionic Hubbard model with density-dependent hopping, [arXiv:2304.04563](#) [cond-mat.str-el].
- [49] L.-F. Lin, Y. Zhang, G. Alvarez, M. A. McGuire, A. F. May, A. Moreo, and E. Dagotto, Stability of the interorbital-hopping mechanism for ferromagnetism in multi-orbital Hubbard models, *Commun. Phys.* **6**, 199 (2023).
- [50] D. Buterakos and S. D. Sarma, Magnetic phases of bilayer quantum-dot Hubbard model plaquettes, *Phys. Rev. B* **108**, 235301 (2023).
- [51] K. J. Kapcia and J. Barański, Magnetic and charge orders on the triangular lattice: Extended hubbard model with intersite ising-like magnetic interactions in the atomic limit, *J. Magn. Magn. Mater.* **591**, 171702 (2024).
- [52] C. Feng, E. Ibarra-García-Padilla, K. R. A. Hazzard, R. Scalettar, S. Zhang, and E. Vitali, Metal-insulator transition and quantum magnetism in the SU(3) Fermi-Hubbard model: Disentangling nesting and the mott transition, *Phys. Rev. Res.* **5**, 043267 (2023).
- [53] M. Gall, N. Wurz, J. Samland, C. F. Chan, and M. Köhl, Competing magnetic orders in a bilayer Hubbard model with ultracold atoms, *Nature (London)* **589**, 40 (2021).
- [54] I. Affleck and J. B. Marston, Large- $n$  limit of the Heisenberg-Hubbard model: Implications for high-  $T_c$  superconductors, *Phys. Rev. B* **37**, 3774(R) (1988).
- [55] V. Gilmutdinov, M. Timirgazin, and A. Arzhnikov, Interplay of magnetism and superconductivity in 2D extended Hubbard model, *J. Magn. Magn. Mater.* **560**, 169605 (2022).
- [56] W.-C. Chen, Y. Wang, and C.-C. Chen, Superconducting phases of the square-lattice extended Hubbard model, *Phys. Rev. B* **108**, 064514 (2023).
- [57] G. D. Adebanjo, J. P. Hague, and P. E. Kornilovitch, Ubiquity of light small pairs in Hubbard models with long range hoppings and interactions, *Phys. Lett. A* **507**, 129474 (2024).
- [58] S. Kundu and D. Sénéchal, CDMFT+HFD : An extension of dynamical mean field theory for nonlocal interactions applied to the single band extended Hubbard model, [arXiv:2310.16075](#) [cond-mat.str-el].
- [59] K. Wrześniowski, T. Ślusarski, and I. Weymann, Nonmonotonic buildup of spin-singlet correlations in a double quantum dot, *Phys. Rev. B* **108**, 144307 (2023).
- [60] P. Frey, L. Hackl, and S. Rachel, Hilbert space fragmentation and interaction-induced localization in the extended Fermi-Hubbard model, *Phys. Rev. B* **106**, L220301 (2022).
- [61] A. Nico-Katz, G. Jaliel, P. Atkinson, T. A. Mitchell, D. A. Ritchie, C. G. Smith, and S. Bose, Identifying many-body localization in realistic dot arrays, [arXiv:2301.08246](#) [cond-mat.dis-nn].
- [62] E. W. Huang, C. B. Mendl, H.-C. Jiang, B. Moritz, and T. P. Devereaux, Stripe order from the perspective of the Hubbard model, *npj Quantum Mater.* **3**, 22 (2018).
- [63] L. Philoxene, V. H. Dao, and R. Frésard, Spin and charge modulations of a half-filled extended Hubbard model, *Phys. Rev. B* **106**, 235131 (2022).
- [64] S. dos Anjos Sousa-Júnior, N. C. Costa, and R. R. dos Santos, Half-filled extended Hubbard model on a square lattice: Phase boundaries from determinant quantum Monte Carlo simulations, *Phys. Rev. B* **109**, 165102 (2024).
- [65] F. Gebhard, K. Bauerbach, and O. Legeza, Generic Mott-Hubbard phase diagram for extended Hubbard models without umklapp scattering, *Phys. Rev. B* **108**, 205130 (2023).
- [66] T. Botzung and P. Nataf, Exact diagonalization of SU( $N$ ) Fermi-Hubbard models, *Phys. Rev. Lett.* **132**, 153001 (2024).
- [67] S. Juliá-Farré, L. Cardarelli, M. Lewenstein, M. Müller, and A. Dauphin, Topological stripe state in an extended Fermi-Hubbard model, *Phys. Rev. B* **109**, 075109 (2024).
- [68] T. Dvir, G. Wang, N. van Loo, C.-X. Liu, G. P. Mazur, A. Bordin, S. L. D. ten Haaf, J.-Y. Wang, D. van Driel, F. Zatelli, X. Li, F. K. Malinowski, S. Gazibegovic, G. Badawy, E. P. A. M. Bakkers, M. Wimmer, and L. P. Kouwenhoven, Realization of a minimal Kitaev chain in coupled quantum dots, *Nature (London)* **614**, 445 (2023).
- [69] A. Bordin, X. Li, D. van Driel, J. C. Wolff, Q. Wang, S. L. D. ten Haaf, G. Wang, N. van Loo, L. P. Kouwenhoven, and T. Dvir, Crossed Andreev reflection and elastic cotunneling in three quantum dots coupled by superconductors, *Phys. Rev. Lett.* **132**, 056602 (2024).
- [70] M. Mansouri, V. Mughnetsyan, A. Manaselyan, A. Kirakosyan, V. Gudmundsson, and V. Aziz-Aghchegala, Hofstadter-like spectrum and magnetization of artificial graphene constructed with cylindrical and elliptical quantum dots, *Phys. Lett. A* **487**, 129115 (2023).
- [71] J. Salfi, J. A. Mol, R. Rahman, G. Klimeck, M. Y. Simmons, L. C. L. Hollenberg, and S. Rogge, Quantum simulation of the Hubbard model with dopant atoms in silicon, *Nat. Commun.* **7**, 11342 (2016).

- [72] A. Dusko, A. Delgado, A. Saraiva, and B. Koiller, Adequacy of Si:P chains as Fermi–Hubbard simulators, *npj Quantum Inf.* **4**, 1 (2018).
- [73] C. J. van Diepen, T.-K. Hsiao, U. Mukhopadhyay, C. Reichl, W. Wegscheider, and L. M. K. Vandersypen, Quantum simulation of antiferromagnetic Heisenberg chain with gate-defined quantum dots, *Phys. Rev. X* **11**, 041025 (2021).
- [74] Y. P. Kandel, H. Qiao, S. Fallahi, G. C. Gardner, M. J. Manfra, and J. M. Nichol, Adiabatic quantum state transfer in a semiconductor quantum-dot spin chain, *Nat. Commun.* **12**, 2156 (2021).
- [75] A. M. J. Zwerver, S. V. Amitonov, S. L. de Snoo, M. T. Mądzik, M. Rimbach-Russ, A. Sammak, G. Scappucci, and L. M. K. Vandersypen, Shuttling an electron spin through a silicon quantum dot array, *PRX Quantum* **4**, 030303 (2023).
- [76] A. R. Mills, D. M. Zajac, M. J. Gullans, F. J. Schupp, T. M. Hazard, and J. R. Petta, Shutting a single charge across a one-dimensional array of silicon quantum dots, *Nat. Commun.* **10**, 1063 (2019).
- [77] J. Yoneda, W. Huang, M. Feng, C. H. Yang, K. W. Chan, T. Tanttu, W. Gilbert, R. C. C. Leon, F. E. Hudson, K. M. Itoh, A. Morello, S. D. Bartlett, A. Laucht, A. Saraiva, and A. S. Dzurak, Coherent spin qubit transport in silicon, *Nat. Commun.* **12**, 4114 (2021).
- [78] T. Utsugi, T. Kuno, N. Lee, R. Tsuchiya, T. Mine, D. Hisamoto, S. Saito, and H. Mizuno, Single electron routing in a silicon quantum-dot array, *Phys. Rev. B* **108**, 235308 (2023).
- [79] H. Qiao, Y. P. Kandel, S. Fallahi, G. C. Gardner, M. J. Manfra, X. Hu, and J. M. Nichol, Long-distance superexchange between semiconductor quantum-dot electron spins, *Phys. Rev. Lett.* **126**, 017701 (2021).
- [80] C. Volk, A. M. J. Zwerver, U. Mukhopadhyay, P. T. Eendebak, C. J. van Diepen, J. P. Dehollain, T. Hengsens, T. Fujita, C. Reichl, W. Wegscheider, and L. M. K. Vandersypen, Loading a quantum-dot based “Qubyte” register, *npj Quantum Inf.* **5**, 29 (2019).
- [81] L. Gaudreau, S. A. Studenikin, A. S. Sachrajda, P. Zawadzki, A. Kam, J. Lapointe, M. Korkusinski, and P. Hawrylak, Stability diagram of a few-electron triple dot, *Phys. Rev. Lett.* **97**, 036807 (2006).
- [82] M. D. Reed, B. M. Maune, R. W. Andrews, M. G. Borselli, K. Eng, M. P. Jura, A. A. Kiselev, T. D. Ladd, S. T. Merkel, I. Milosavljevic, E. J. Pritchett, M. T. Rakher, R. S. Ross, A. E. Schmitz, A. Smith, J. A. Wright, M. F. Gyure, and A. T. Hunter, Reduced sensitivity to charge noise in semiconductor spin qubits via symmetric operation, *Phys. Rev. Lett.* **116**, 110402 (2016).
- [83] M. Meyer, C. Déprez, T. R. van Abswoude, I. N. Meijer, D. Liu, C.-A. Wang, S. Karwal, S. Oosterhout, F. Borsoi, A. Sammak, N. W. Hendrickx, G. Scappucci, and M. Veldhorst, Electrical control of uniformity in quantum dot devices, *Nano Lett.* **23**, 2522 (2023).
- [84] B. Sun, T. Brecht, B. Fong, M. Akmal, J. Z. Blumoff, T. A. Cain, F. W. Carter, D. H. Finestone, M. N. Fireman, W. Ha, A. T. Hatke, R. M. Hickey, C. A. C. Jackson, I. Jenkins, A. M. Jones, A. Pan, D. R. Ward, A. J. Weinstein, S. J. Whiteley, P. Williams *et al.*, Full-permutation dynamical decoupling in triple-quantum-dot spin qubits, [arXiv:2208.11784](https://arxiv.org/abs/2208.11784) [quant-ph].
- [85] J. D. Cifuentes, T. Tanttu, P. Steinacker, S. Serrano, I. Hansen, J. P. Slack-Smith, W. Gilbert, J. Y. Huang, E. Vahapoglu, R. C. C. Leon, N. D. Stuyck, K. Itoh, N. Abrosimov, H.-J. Pohl, M. Thewalt, A. Laucht, C. H. Yang, C. C. Escott, F. E. Hudson, W. H. Lim *et al.*, Impact of electrostatic crosstalk on spin qubits in dense CMOS quantum dot arrays, [arXiv:2309.01849](https://arxiv.org/abs/2309.01849) [cond-mat.mes-hall].
- [86] P.-A. Mortemousque, E. Chanrion, B. Jadot, H. Flentje, A. Ludwig, A. D. Wieck, M. Urdampilleta, C. Bäuerle, and T. Meunier, Coherent control of individual electron spins in a two-dimensional quantum dot array, *Nat. Nanotechnol.* **16**, 296 (2021).
- [87] C. J. van Diepen, T.-K. Hsiao, U. Mukhopadhyay, C. Reichl, W. Wegscheider, and L. M. K. Vandersypen, Electron cascade for distant spin readout, *Nat. Commun.* **12**, 77 (2021).
- [88] F. Ansaloni, A. Chatterjee, H. Bohuslavskyi, B. Bertrand, L. Hutin, M. Vinet, and F. Kuemmeth, Single-electron operations in a foundry-fabricated array of quantum dots, *Nat. Commun.* **11**, 6399 (2020).
- [89] N. H. Le, A. J. Fisher, and E. Ginossar, Extended Hubbard model for mesoscopic transport in donor arrays in silicon, *Phys. Rev. B* **96**, 245406 (2017).
- [90] W. I. L. Lawrie, H. G. J. Eenink, N. W. Hendrickx, J. M. Boter, L. Petit, S. V. Amitonov, M. Lodari, B. Paquelet Wuetz, C. Volk, S. G. J. Philips, G. Droulers, N. Kalhor, F. van Riggelen, D. Brousse, A. Sammak, L. M. K. Vandersypen, G. Scappucci, and M. Veldhorst, Quantum dot arrays in silicon and germanium, *Appl. Phys. Lett.* **116**, 080501 (2020).
- [91] X. Wang, E. Khatami, F. Fei, J. Wyrick, P. Namboodiri, R. Kashid, A. F. Rigos, G. Bryant, and R. Silver, Experimental realization of an extended Fermi-Hubbard model using a 2D lattice of dopant-based quantum dots, *Nat. Commun.* **13**, 6824 (2022).
- [92] P.-A. Mortemousque, B. Jadot, E. Chanrion, V. Thiney, C. Bäuerle, A. Ludwig, A. D. Wieck, M. Urdampilleta, and T. Meunier, Enhanced spin coherence while displacing electron in a two-dimensional array of quantum dots, *PRX Quantum* **2**, 030331 (2021).
- [93] R. E. Throckmorton and S. Das Sarma, Crosstalk- and charge-noise-induced multiqubit decoherence in exchange-coupled quantum dot spin qubit arrays, *Phys. Rev. B* **105**, 245413 (2022).
- [94] F. Borsoi, N. W. Hendrickx, V. John, M. Meyer, S. Motz, F. van Riggelen, A. Sammak, S. L. de Snoo, G. Scappucci, and M. Veldhorst, Shared control of a 16 semiconductor quantum dot crossbar array, *Nat. Nanotechnol.* **19**, 21 (2024).
- [95] D. K. Campbell, J. T. Gammel, and E. Y. Loh, Bond-charge coulomb repulsion in Peierls-Hubbard models, *Phys. Rev. B* **38**, 12043 (1988).
- [96] D. K. Campbell, J. Tinka Gammel, and E. Y. Loh, Jr., Modeling electron-electron interactions in reduced-dimensional materials: Bond-charge Coulomb repulsion and dimerization in Peierls-Hubbard models, *Phys. Rev. B: Condensed Matter* **42**, 475 (1990).
- [97] S. Kivelson, W.-P. Su, J. R. Schrieffer, and A. J. Heeger, Missing bond-charge repulsion in the extended Hubbard model: Effects in polyacetylene, *Phys. Rev. Lett.* **58**, 1899 (1987).
- [98] S. Yang, X. Wang, and S. Das Sarma, Generic Hubbard model description of semiconductor quantum-dot spin qubits, *Phys. Rev. B* **83**, 161301(R) (2011).

- [99] H. Overweg, H. Eggemann, X. Chen, S. Slizovskiy, M. Eich, R. Pisoni, Y. Lee, P. Rickhaus, K. Watanabe, T. Taniguchi, V. Fal'ko, T. Ihn, and K. Ensslin, Electrostatically induced quantum point contacts in bilayer graphene, *Nano Lett.* **18**, 553 (2018).
- [100] Y. Lee, A. Knothe, H. Overweg, M. Eich, C. Gold, A. Kurzmann, V. Klasovika, T. Taniguchi, K. Wantanabe, V. Fal'ko, T. Ihn, K. Ensslin, and P. Rickhaus, Tunable valley splitting due to topological orbital magnetic moment in bilayer graphene quantum point contacts, *Phys. Rev. Lett.* **124**, 126802 (2020).
- [101] H. Overweg, A. Knothe, T. Fabian, L. Linhart, P. Rickhaus, L. Wernli, K. Watanabe, T. Taniguchi, D. Sánchez, J. Burgdörfer, F. Libisch, V. I. Fal'ko, K. Ensslin, and T. Ihn, Topologically nontrivial valley states in bilayer graphene quantum point contacts, *Phys. Rev. Lett.* **121**, 257702 (2018).
- [102] C. Yannouleas and U. Landman, Barriers and deformation in fission of charged metal clusters, *J. Phys. Chem.* **99**, 14577 (1995).
- [103] C. Yannouleas and U. Landman, Coupling and dissociation in artificial molecules, *Eur. Phys. J. D* **16**, 373 (2001).
- [104] C. Yannouleas and U. Landman, Spontaneous symmetry breaking in single and molecular quantum dots, *Phys. Rev. Lett.* **82**, 5325 (1999).
- [105] C. Yannouleas and U. Landman, Strongly correlated wavefunctions for artificial atoms and molecules, *J. Phys.: Condens. Matter* **14**, L591 (2002).
- [106] U. Mosel and H. W. Schmitt, Fragment-shell influences in nuclear fission, *Phys. Rev. C* **4**, 2185 (1971).
- [107] M. G. Mustafa, U. Mosel, and H. W. Schmitt, Asymmetry in nuclear fission, *Phys. Rev. C* **7**, 1518 (1973).
- [108] E. McCann, D. S. Abergel, and V. I. Fal'ko, The low energy electronic band structure of bilayer graphene, *Eur. Phys. J.: Spec. Top.* **148**, 91 (2007).
- [109] E. McCann and M. Koshino, The electronic properties of bilayer graphene, *Rep. Prog. Phys.* **76**, 056503 (2013).
- [110] H. Ochoa, A. H. Castro Neto, V. I. Fal'ko, and F. Guinea, Spin-orbit coupling assisted by flexural phonons in graphene, *Phys. Rev. B* **86**, 245411 (2012).
- [111] L. Banszerus, B. Frohn, T. Fabian, S. Somanchi, A. Epping, M. Müller, D. Neumaier, K. Watanabe, T. Taniguchi, F. Libisch, B. Beschoten, F. Hassler, and C. Stampfer, Observation of the spin-orbit gap in bilayer graphene by one-dimensional ballistic transport, *Phys. Rev. Lett.* **124**, 177701 (2020).
- [112] V. V. Cheianov, I. L. Aleiner, and V. I. Fal'ko, Gapped bilayer graphene: A tunable strongly correlated band insulator, *Phys. Rev. Lett.* **109**, 106801 (2012).
- [113] M. Kharitonov, Canted antiferromagnetic phase of the  $\nu = 0$  quantum Hall state in bilayer graphene, *Phys. Rev. Lett.* **109**, 046803 (2012).
- [114] M. Kharitonov, Phase diagram for the  $\nu = 0$  quantum Hall state in monolayer graphene, *Phys. Rev. B* **85**, 155439 (2012).
- [115] Y. Lemonik, I. Aleiner, and V. I. Fal'ko, Competing nematic, antiferromagnetic, and spin-flux orders in the ground state of bilayer graphene, *Phys. Rev. B* **85**, 245451 (2012).
- [116] B. Ganchev, N. Drummond, I. Aleiner, and V. Fal'ko, Three-particle complexes in two-dimensional semiconductors, *Phys. Rev. Lett.* **114**, 107401 (2015).
- [117] I. L. Aleiner, D. E. Kharzeev, and A. M. Tsvelik, Spontaneous symmetry breaking in graphene subjected to an in-plane magnetic field, *Phys. Rev. B* **76**, 195415 (2007).
- [118] A. Knothe and V. Fal'ko, Influence of minivalleys and Berry curvature on electrostatically induced quantum wires in gapped bilayer graphene, *Phys. Rev. B* **98**, 155435 (2018).
- [119] D. Xiao, M.-C. Chang, and Q. Niu, Berry phase effects on electronic properties, *Rev. Mod. Phys.* **82**, 1959 (2010).
- [120] C. Moultsdale, A. Knothe, and V. Fal'ko, Engineering of the topological magnetic moment of electrons in bilayer graphene using strain and electrical bias, *Phys. Rev. B* **101**, 085118 (2020).
- [121] C.-S. Park, Valley filtering due to orbital magnetic moment in bilayer graphene, *Phys. Lett. A* **382**, 121 (2017).
- [122] J. N. Fuchs, F. Piéchon, M. O. Goerbig, and G. Montambaux, Topological Berry phase and semiclassical quantization of cyclotron orbits for two dimensional electrons in coupled band models, *Eur. Phys. J. B* **77**, 351 (2010).
- [123] N. Morales-Durán, N. C. Hu, P. Potasz, and A. H. MacDonald, Nonlocal interactions in Moiré Hubbard systems, *Phys. Rev. Lett.* **128**, 217202 (2022).
- [124] N. Götting, F. Lohof, and C. Gies, Moiré-Bose-Hubbard model for interlayer excitons in twisted transition metal dichalcogenide heterostructures, *Phys. Rev. B* **105**, 165419 (2022).
- [125] O. Dutta, M. Gajda, P. Hauke, M. Lewenstein, D.-S. Lühmann, B. A. Malomed, T. Sowiński, and J. Zakrzewski, Non-standard Hubbard models in optical lattices: A review, *Rep. Prog. Phys.* **78**, 066001 (2015).
- [126] O. Jürgensen, K. Sengstock, and D.-S. Lühmann, Density-induced processes in quantum gas mixtures in optical lattices, *Phys. Rev. A* **86**, 043623 (2012).
- [127] M. Zendra, F. Borgonovi, G. L. Celardo, and S. Gurvitz, Non-standard Hubbard model and two-electron pairing, *Phys. Rev. B* **109**, 195137 (2024).
- [128] G. Kiršanskas, J. N. Pedersen, O. Karlström, M. Leijnse, and A. Wacker, QmeQ 1.0: An open-source Python package for calculations of transport through quantum dot devices, *Comput. Phys. Commun.* **221**, 317 (2017).
- [129] A. Laturia, M. L. Van de Put, and W. G. Vandenberghe, Dielectric properties of hexagonal boron nitride and transition metal dichalcogenides: From monolayer to bulk, *npj 2D Mater Appl* **2**, 6 (2018).
- [130] M. E. Levinshtein, S. L. Rumyantsev, and M. S. Shur, *Properties of Advanced Semiconductor Materials: GaN, AlN, InN, BN, SiC, SiGe* (John Wiley & Sons, New York, Chichester, 2001).
- [131] A. Pályi and G. Burkard, Hyperfine-induced valley mixing and the spin-valley blockade in carbon-based quantum dots, *Phys. Rev. B* **80**, 201404(R) (2009).
- [132] A. David, G. Burkard, and A. Kormányos, Effective theory of monolayer TMDC double quantum dots, *2D Mater.* **5**, 035031 (2018).
- [133] F. Pei, E. A. Laird, G. A. Steele, and L. P. Kouwenhoven, Valley–spin blockade and spin resonance in carbon nanotubes, *Nat. Nanotechnol.* **7**, 630 (2012).
- [134] F. Martins, F. K. Malinowski, P. D. Nissen, S. Fallahi, G. C. Gardner, M. J. Manfra, C. M. Marcus, and F. Kuemmeth, Negative spin exchange in a multielectron quantum dot, *Phys. Rev. Lett.* **119**, 227701 (2017).

- [135] K. Deng, F. A. Calderon-Vargas, N. J. Mayhall, and E. Barnes, Negative exchange interactions in coupled few-electron quantum dots, *Phys. Rev. B* **97**, 245301 (2018).
- [136] D. Culcer, X. Hu, and S. Das Sarma, Dephasing of Si spin qubits due to charge noise, *Appl. Phys. Lett.* **95**, 073102 (2009).
- [137] J. M. Pizarro, M. Rösner, R. Thomale, R. Valentí, and T. O. Wehling, Internal screening and dielectric engineering in magic-angle twisted bilayer graphene, *Phys. Rev. B* **100**, 161102(R) (2019).
- [138] E. G. C. P. van Loon, M. Schüler, D. Springer, G. Sangiovanni, J. M. Tomczak, and T. O. Wehling, Coulomb engineering of two-dimensional Mott materials, *npj 2D Mater. Appl.* **7**, 47 (2023).
- [139] P. Steinleitner, P. Merkl, A. Graf, P. Nagler, K. Watanabe, T. Taniguchi, J. Zipfel, C. Schüller, T. Korn, A. Chernikov, S. Brem, M. Selig, G. Berghäuser, E. Malic, and R. Huber, Dielectric engineering of electronic correlations in a van der waals heterostructure, *Nano Lett.* **18**, 1402 (2018).